



## City Research Online

### City, University of London Institutional Repository

---

**Citation:** Sahin, B., Bravo-Haro, M. A. & Elghazouli, A. Y. (2022). Assessment of cyclic degradation effects in composite steel-concrete members. *Journal of Constructional Steel Research*, 192, 107231. doi: 10.1016/j.jcsr.2022.107231

This is the published version of the paper.

This version of the publication may differ from the final published version.

---

**Permanent repository link:** <https://openaccess.city.ac.uk/id/eprint/29737/>

**Link to published version:** <https://doi.org/10.1016/j.jcsr.2022.107231>

**Copyright:** City Research Online aims to make research outputs of City, University of London available to a wider audience. Copyright and Moral Rights remain with the author(s) and/or copyright holders. URLs from City Research Online may be freely distributed and linked to.

**Reuse:** Copies of full items can be used for personal research or study, educational, or not-for-profit purposes without prior permission or charge. Provided that the authors, title and full bibliographic details are credited, a hyperlink and/or URL is given for the original metadata page and the content is not changed in any way.

---

---

---

City Research Online:

<http://openaccess.city.ac.uk/>

[publications@city.ac.uk](mailto:publications@city.ac.uk)

---



# Assessment of cyclic degradation effects in composite steel-concrete members

B. Sahin<sup>a</sup>, M.A. Bravo-Haro<sup>b</sup>, A.Y. Elghazouli<sup>a,\*</sup>

<sup>a</sup> Department of Civil and Environmental Engineering, Imperial College London, UK

<sup>b</sup> Centre for Smart Infrastructure and Construction, Engineering Department, University of Cambridge, UK

## ARTICLE INFO

### Keywords:

Composite steel-concrete members  
Seismic behaviour  
Cyclic degradation

## ABSTRACT

This paper investigates the inelastic behaviour of composite steel concrete beams, with particular emphasis on cyclic deterioration effects. A detailed continuum model is firstly developed to represent the hysteretic response of composite steel beam and concrete slab assemblages, validated against available experimental cyclic results on both steel and composite members. The proposed model is then adopted to perform detailed parametric assessments which are used to gain insights into the key response characteristics related to the inelastic cyclic performance of composite steel/concrete members, including their stiffness, capacity, and ductility. A synthetically generated numerical database is subsequently used to develop relationships governing the plastic rotation and cyclic degradation of dissipative composite beams as a function of the main geometric and material properties, with focus on members designed to European codified procedures. The deterioration effects are shown to be dependent on a number of key factors including, most significantly, the composite beam depth and the steel cross-section slenderness. In addition to the asymmetry in behaviour under sagging and hogging moments, it is shown that composite members typically exhibit 20% more degradation under cyclic loading compared to their bare steel counterparts. Importantly, the proposed cyclic degradation expressions for composite beams also enable the calibration of widely used uniaxial deterioration models which are suitable for implementation in computationally efficient nonlinear inelastic frame analysis for structural systems. These expressions also provide fundamental information required for idealised pushover representations for practical seismic assessment and design purposes.

## 1. Introduction

Satisfactory performance of multi-storey framed buildings under extreme seismic events relies on the formation of favourable plastic mechanisms coupled with adequate ductility and energy dissipation within key zones through the application of capacity design procedures [1]. In addition to the need to evaluate the stiffness, strength and ductility properties, appropriate assessment of the seismic performance necessitates a detailed understanding of the characteristic cyclic behaviour of dissipative zones. In the case of moment resisting frames, such dissipative zones predominantly occur in the beams in accordance with the weak beam-strong column concept.

The use of composite action between steel beams and concrete floor slabs offers various behavioural and constructional merits compared to bare steel or reinforced concrete counterparts. Composite action can lead to significant enhancements in the flexural stiffness and strength,

and hence enables the use of frame systems with relatively large spans and reduced overall floor depth. The synergetic combination of steel and concrete can also result in behavioural benefits in terms of mitigating local instabilities in steel and more effective mobilisation of the compressive strength of concrete constituents.

A number of experimental investigations have examined the cyclic behaviour of systems consisting of steel beams and reinforced concrete slabs, including conventional and reduced beam forms, e.g. [2–6]. However, most tests were either without shear studs in the vicinity of the column, hence intended as steel beams with protected zones, in accordance with US seismic code provisions [7], or with low levels of composite interaction which do not conform to composite dissipative requirements in European seismic provisions [8]. Many tested specimens also adopted relatively deep steel cross-sections, common in US design practice for perimeter moment frames, in contrast to typical European practice in which shallower beams and internal moment frames are often employed. Whilst available test results provide valuable

\* Corresponding author.

E-mail address: [a.elghazouli@imperial.ac.uk](mailto:a.elghazouli@imperial.ac.uk) (A.Y. Elghazouli).

**Nomenclature**

The following notations apply in this paper.

**Abbreviations**

BS	Bare steel
CDP	Concrete damage plasticity
CFST	Concrete filled steel tube
CS	Composite specimen
FEA	Finite element analysis
FLB	Flange local buckling
LTB	Lateral torsional buckling
NRMSE	Normalised root mean square error
RBS	Reduced beam section
SCWB	Strong column weak beam

**Uppercase Latin letters**

$A_c$	Cross-sectional area of the concrete flange
$A_{eq}$	Equivalent steel cross-section area
$A_s$	Cross-sectional area of the steel section
$D^{+/-}$	Rate of cyclic deterioration in positive/negative directions
$I_{eq}$	Equivalent moment of inertia
$K_{eq}$	Initial equivalent stiffness of composite beam
$K_{steel}$	Stiffness of steel beam
$L$	Length of beam
$L_b$	Unrestrained distance from support
$M_c^{+/-}$	Ultimate capacity of composite beam for positive/negative loading directions
$M_r^{+/-}$	Residual strength for positive/negative loading directions
$M_y^{+/-}$	Yield moment of composite beam for positive/negative loading directions
$M_{y, steel}$	Yield moment of steel beam
$R_r$	Total strength of the reinforcement bars within the effective width
$R_s$	Axial strength of structural steel

**Lowercase Latin letters**

$b$	Width of steel beam flange
-----	----------------------------

$b_{eff}$	Total effective width of concrete flange acting compositely with the steel beam
$c$	Clear width of steel beam flange
$d$	Clear depth of steel beam web, damage parameter for concrete
$f$	Maximum tensile or compressive strength
$f_{cd}$	Compressive strength of concrete
$f_{yd}$	Yield strength of structural steel
$h$	Depth of composite section
$h_a$	Depth of steel beam
$h_f$	Depth of concrete slab
$i_z$	Radius of gyration
$n$	Modular ratio
$r$	Root fillet radius
$t_w$	Web thickness
$t_f$	Flange thickness
$w$	Crack displacement

**Greek letters**

$\varepsilon$	Strain
$\theta_p^{+/-}$	Pre-capping plastic rotation for positive/negative loading directions
$\theta_{pc}^{+/-}$	Post-capping rotation for positive/negative loading directions
$\theta_{p, pred}^{+/-}$	Plastic rotation capacity for positive/negative loading directions calculated using proposed formulations
$\theta_{p, 80\%}^{+/-}$	Plastic rotation capacity for positive/negative loading directions according to EC8 Part 3 and existing compared papers
$\theta_u^{+/-}$	Ultimate rotation capacity
$\theta_y$	Chord rotation at yield
$\Lambda$	Cyclic deterioration parameter
$\Lambda_{pred}$	Cyclic deterioration parameter calculated by using proposed equation
$\sigma$	Stress

data for validation purposes, they are limited in terms of the range of geometric and material properties, particularly for fully connected composite beams subjected to cyclic loading.

On the numerical side, extensive investigations have been carried out to simulate the behaviour of composite beams. Many previous studies focused on assessing the moment capacity and interaction between steel beams and concrete slabs, mostly under monotonic loading [9–17]. Huang, et al. [18] also performed a numerical parametric study on the effects of concrete slabs on the behaviour of reduced beam section (RBS) connections. Only the sagging bending case was investigated under monotonic loading, and it was shown that the main parameters influencing the behaviour were the depth of the steel and concrete components along with the RBS cut depth. More recently, Rossi, et al. [19] assessed the monotonic behaviour of steel-concrete composite beams under hogging bending with focus on out of plane instabilities, and concluded that the steel cross-section and the presence of web stiffeners had the most influence.

Several studies additionally focused on assessing various parameters related to the seismic response and design of composite beam members. These included the effective slab width, shear interaction, and beam-to-column connection design [20–24]. These studies provided valuable information on the overall stiffness, strength and ductility of composite members and connections. Importantly, it was shown that although composite frames with partial beam-slab connections could be used in seismic design, the shear connectors may be susceptible to premature

fracture failures under cyclic loading [20]. Accordingly, full or near-full beam-slab connection is typically recommended in some seismic codes such as in EC8 [8].

In recognition of the importance of quantifying cyclic degradation effects, Elkady and Lignos [25] proposed a modified version of the Ibarra-Medina-Krawinkler (IMK) cyclic material model initially developed for steel members [26–28]. This model was calibrated using a best fit representation from existing test results on composite beams, combining various partial shear interaction levels and incorporating relatively deep steel beams, typical of North American practice, with and without reduced beam sections. The study concluded that the slab generally increases the sagging resistance by about 35%, irrespective of the type of beam-to-column connection or the degree of composite action, and highlighted the asymmetric sagging/hogging cyclic degradation effects that occur in composite beams. This was followed by other related studies [29,30] which compared the results obtained from the experimental database in terms of strength and rotation capacity with the provisions of European [8,31–33], US [34] and Japanese [35] codes. One of the key conclusions was that EC8-Part3 [33] consistently overestimates the positive and negative rotation capacities by around 50%, noting that the code ignores the effects of geometric and material nonlinearities on the rotation capacity of steel beams.

Although quantifying cyclic degradation is relevant for assessing the ductility capacity of dissipative members, it is of even more importance in predicting the demands under seismic loading. Whilst many studies

have been carried out on assessing seismic demands in steel frames designed to European code provisions (e.g. [36–39], including due consideration for cyclic degradation [40,41], less attention has been given to composite frames [42], particularly those designed to EC8, and with a lack of investigations on the influence of cyclic degradation. This is of crucial importance, as previous studies on steel moment frames have shown that cyclic deterioration can change both the levels of peak demands as well as their distributions within the structure. However, examining the seismic response of composite framed structures requires the development of reliable and efficient frame analysis models that can represent accurately the cyclic degradation effects.

This paper firstly describes a detailed continuum finite element model, which is constructed and validated against test results. Particular attention is given to the suitability of the model in simulating the inelastic cyclic performance of both steel and composite members with due account for cyclic degradation phenomena. The model is then used to perform detailed parametric assessments in order to identify the key properties affecting the cyclic performance as well as to provide a wider database of results covering various geometric and material characteristics, with focus on members designed according to European code provisions.

To enable future detailed studies on composite multi-storey frames, the generated numerical results are used to calibrate a deterioration model based on the underlying relationships governing the plastic rotation and cyclic degradation of composite beams. The proposed cyclic degradation relationships enable the calibration of widely used uniaxial deterioration models which are suitable for implementation in computationally efficient nonlinear inelastic frame analysis for structural systems. A flowchart of the methodology followed in this research, as well as the relationship between the various models and procedures adopted, is illustrated in Fig. 1 and referred to below where relevant.

## 2. Continuum finite element assessments

This section describes the continuum numerical models constructed using the nonlinear finite element analysis (FEA) program ABAQUS [43] in order to widen the database of cyclic results through an extended range of geometric and material properties. As mentioned before, and as illustrated in Fig. 1, this serves the purpose of providing adequate information for the calibration of more efficient degradation models that can be employed in beam element representations within frame analysis. The continuum modelling procedures are validated through comparison with the results of various available cyclic tests on steel and composite steel/concrete configurations. The experimental studies used for validation are firstly described below, followed by the modelling procedures adopted, including the constitutive material models and element types. Comparisons between the numerical and experimental results are then presented, and the parameters considered for generating the synthetic database of numerical results, discussed in subsequent parts of this paper, are introduced.

### 2.1. Validation configurations

Validation of the continuum models was firstly performed against cyclic tests on bare steel specimens in order to ensure that the developed model is initially capable of simulating degradation effects in steel members. For this purpose, four different specimens, incorporating fully welded rigid connections and tested in the major axis direction, from two test series [44,45], were selected, as illustrated in Fig. 2. The specimens are referred to herein as BS1 to BS4 (BS refers to bare steel) in Table 1 which gives the sizes of the beam and column members as well as the connection details and material properties. Full details of the test specimens can be found in the original publications [44,45]. The beams

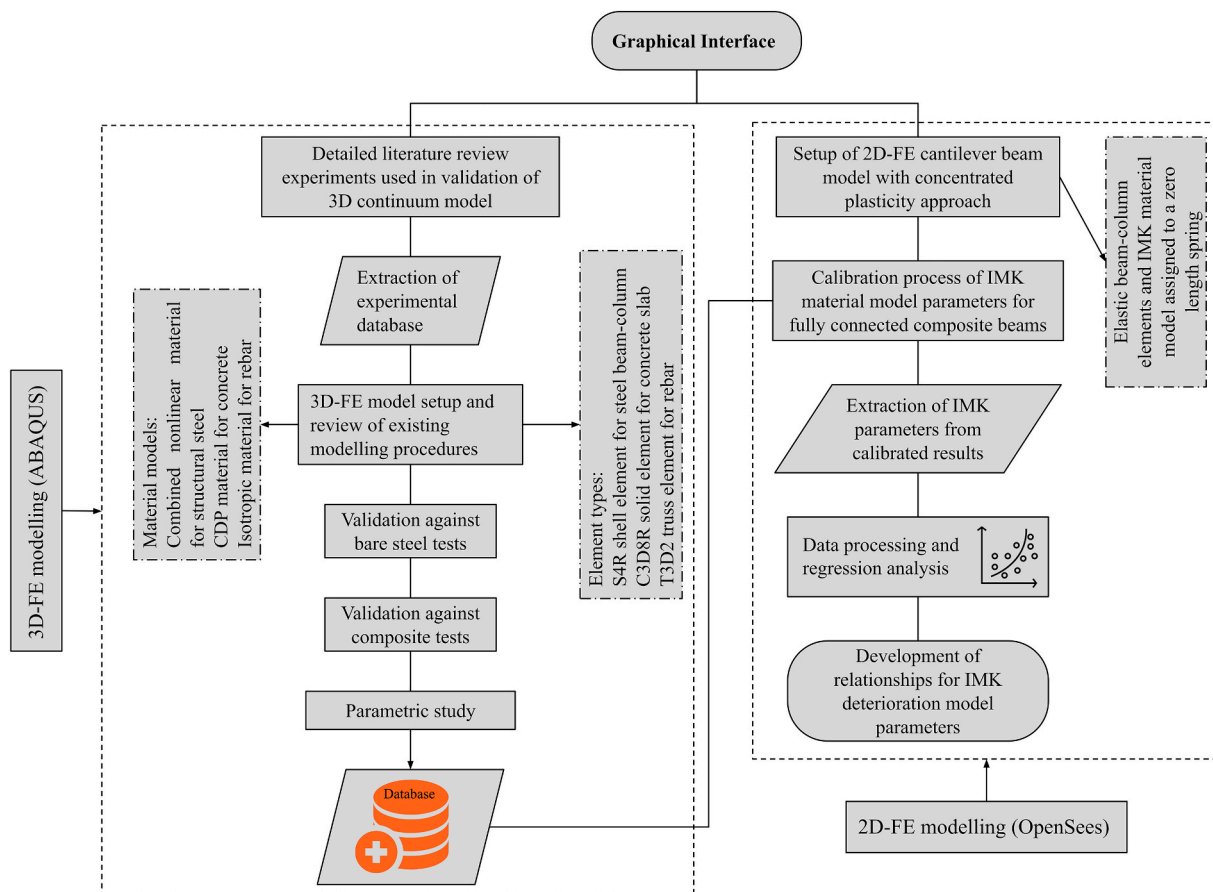


Fig. 1. Flowchart of the methodology used in this study.

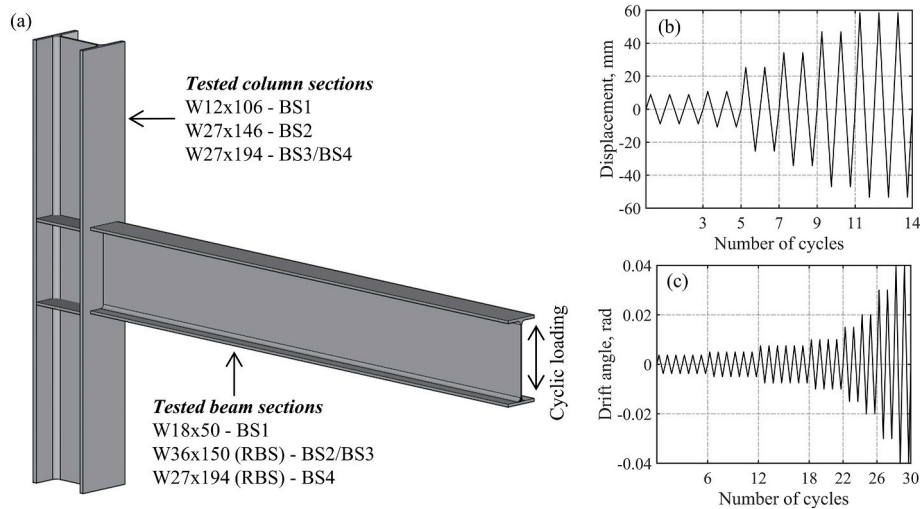


Fig. 2. Schematic test details of bare steel experimental specimens: a) typical test configuration and applied loading histories: b) BS1 [44], and c) BS2 to BS4 [45].

in Specimens BS2 to BS4 had reduced beam sections, while BS1 had a full beam cross section. Table 2 also provides the geometric details of all the structural steel sections used in the tests. During the test for Specimen BS1, a cyclic loading history with arbitrarily selected amplitudes and number of excursions was employed as illustrated in Fig. 2b. As for BS2 to BS4, the standard SAC loading history [46] was applied in the tests as shown in Fig. 2c. For BS1, the failure was gradual with local buckling occurring in the flange, leading to deterioration in the cyclic response thereafter. On the other hand, for BS2-BS4, yielding occurred in the panel zone first, followed by local web buckling in the RBS region, then by flange local buckling and lateral torsional buckling of the steel beam.

For the validation of the models for composite beams, another four specimens referred to herein as CS1 to CS4 (CS denotes a composite specimen) were selected. The details of the composite specimens are given in Table 1, including the beam and column member sizes, concrete slab and connection details, as well as the material properties. Full details of the test specimens can be found in the original publications [47–50]. Geometric details of all structural steel sections used in the experiments are given in Table 2. As noted before, only specimens with full shear connection are considered herein due to the limitations resulting from composite beam design rules in EC4 [32] and EC8 [8]. In EC8, a lower limit of 80% shear connection is stipulated based on previous studies and a 25% reduction of the actual resistance of shear connectors is applied, hence effectively imposing full connection conditions [1].

Specimen CS1 (denoted FC in the original test series), tested by Bursi and Gramola [47], represented an exterior connection and incorporated a profiled composite slab. The length between the column centre line and loading point was 4000 mm, while the vertical distance between the pinned support and loading point was 1400 mm. The reinforcement was doubled in the longitudinal direction in the column region and 2Ø16 rebars were also added around the column in addition to the basic reinforcement mesh of Ø12 rebars with 160 mm and 200 mm spacing in the longitudinal and transverse directions, respectively. The steel column and composite beam section details including material properties as well as connection details are given in Table 1, whilst Table 2 provides the geometric details of steel sections. The behaviour was governed by yielding and local buckling of the bottom flange as well as yielding of the reinforcement bars. Fig. 3a, 3b, and c depict the specimen configuration, composite beam cross-section, and the applied cycling loading protocol [51], respectively.

Another fully-welded internal composite specimen (denoted WR in the original test series) tested by Doneux and Parung [48], and referred

to herein as Specimen CS2, was also used for validation. The specimen configuration together with composite beam cross-section and applied cyclic loading protocol are shown in Fig. 4a, b, and c, with other details given in Tables 1 and 2. The height from the bottom support to the loading point was 2975 mm, and the horizontal distance between the roller supports at the beam ends was 3800 mm. A welded mesh Q513 ( $A = 5.13 \text{ cm}^2/\text{m}$ ) was used in the composite slab, with additional reinforcement of 3Ø10 rebars placed on both sides of the column. The cyclic loading history shown in Fig. 4c was applied at the top of the column up to a storey drift of about 7%. A ductile behaviour was observed in the specimen with local buckling of the bottom flange and crushing of concrete in the slab occurring at large deformation levels.

A further fully-welded composite specimen used for cyclic validation was a one-bay one-storey frame, consisting of steel columns and composite beams, tested by Udagawa and Mimura [49]. The test series included other bare steel frames and specimens tested under pseudo-dynamic conditions. The cyclic composite frame specimen considered is referred to herein as CS3 (denoted CCE-5 in the original test series). The specimen configuration and applied cyclic loading protocol are shown in Fig. 5a to 5c, and other details are given in Tables 1 and 2. The number and space of stud connectors were calculated in order to provide a fully connected composite beam. The composite slab mesh reinforcement was Ø6 with 100 mm spacing. The height of the frames, from the bottom of columns to centre line of the steel beam was 1200 mm, while the bay width between the centre lines of columns was 2900 mm. The cyclic loading history shown in Fig. 5c was applied to the column in the direction of the steel beam axis. The ultimate behaviour involved compressive failure of concrete and local buckling of the steel beam.

The fourth composite specimen was an exterior joint tested with the series examined by Han and Li [50] consisting of a concrete filled steel tube (CFST) column and a steel beam with reinforced concrete solid slab. The column height between two cover plates at both ends and the beam length between column centre line and the loading point were 1500 mm and 1300 mm, respectively. The specimen is referred to herein as CS4 (denoted as CEJ-2 in the original test series). A solid slab was used, with a reinforcement mesh of Ø10 at 100 mm in both directions. The detailed material properties, specimen configuration with applied loading history, and geometric dimensions of the steel members are shown in Table 1, Fig. 6a to 6d and Table 2, respectively. The ultimate behaviour of the specimen involved crushing of the concrete slab and buckling of steel beam flange followed by fracture of connection weld.

The procedures adopted for constructing the detailed continuum models, which are used to simulate the behaviour of the above-described cyclic tests on steel and composite specimens, are discussed below. After

**Table 1**  
Details of experimental studies used for 3D-FE model validation.

Notation	Configuration details		Structural steel sections		Concrete slab geometric details			Material properties				Notation in cited papers	Reference				
	Type of joint	Connection details	Beam	Column	Concrete slab	Type of concrete slab	Width of concrete flange, $b_{eff}$ , mm	Thickness of concrete flange, $h_f$ , mm	Concrete, MPa	Steel beam, MPa							
									$f_{cm}$	$f_{cm}$	$E_{cm}$	Flange	Web				
									$f_y$	$f_y$	$f_u$	$f_y$	$f_y$	$f_u$			
<b>Bare steel specimens</b>																	
BS1	Exterior	Welded	W18x50	W12x106	No	NA	NA	NA	NA	NA	NA	310.3	474.4	504	[44]		
BS2	Exterior	Welded-RBS	W36x150	W27x146	No	NA	NA	NA	NA	NA	NA	400.6	455.7	445.4	DC1		
BS3	Exterior	Welded-RBS	W36x150	W27x194	No	NA	NA	NA	NA	NA	NA	400.6	455.7	445.4	DC2		
BS4	Exterior	Welded-RBS	W27x194	W27x194	No	NA	NA	NA	NA	NA	NA	427.5	453.7	448.8	DC3		
<b>Composite specimens</b>																	
CS1	Exterior	Welded	IPE330	HE360B	Yes		1200	120(55)*	39.0	3.0	32217	291	451	462	FC	[47]	
CS2	Interior	Welded	IPE300	HE260M	Yes	T	3200	120(51)*	31.0	NR	NR	287	447	447	WR	[48]	
CS3	One-bay frame	Welded	200x100x5.5x8	200x200x8x12	Yes	T	900	75(25)*	22.6 (Cylinder)	NR	NR	335	461	391	488	CCE-5	[49]
CS4	Exterior	Welded-External diaphragm	150x100x5.62x5.62	Φ219x4.68 (Circular CFST)	Yes	SS	700	50	35.7	NR	28600	475.4	601.5	467.3	597	GEJ-2	[50]

NA - not available; NR - not reported.  
 || - ribs parallel to the steel beam; T - ribs perpendicular to the steel beam; SS - solid slab.  
 \* Numbers in bracket depict the depth of ribs.

**Table 2**  
Dimensions of steel sections, (in mm).

Section	Depth, $h_a$	Flange width, $b$	Web thickness, $t_w$	Flange thickness, $t_f$
W12x106	327.4	310.4	15.5	25.1
W18x50	456.9	190.4	9.0	14.5
W27x146	695.5	354.7	15.4	24.8
W27x194	714.0	356.5	19.1	34.0
W36x150	910.6	304.2	15.9	23.9
IPE300	300.0	150.0	7.1	10.7
IPE330	330.0	160.0	7.5	11.5
HE260M	290.0	268.0	18.0	32.5
HE360B	360.0	300.0	12.5	22.5
150x100x5.62x5.62	150.0	100.0	5.6	5.6
200x100x5.5x8	200.0	100.0	5.5	8.0
200x200x8x12	200.0	200.0	8.0	12.0
Φ219x4.68	$D =$ 219.0	$t =$ 4.68		

validation by comparison against the experimental results, the continuum models are then employed for undertaking detailed numerical assessments as described in subsequent parts of this study.

**2.2. Modelling procedures**

In the detailed continuum numerical models, the steel beams and columns were simulated by means of 4-node quadratic “S4R” shell elements that use reduced integration and account for shear deformations. They can also capture local buckling within the cross-section. The concrete slab was modelled using 8-node solid elements “C3D8R” with reduced integration and hourglass control, while the reinforcement was modelled discretely using two-node linear truss elements “T3D2” and embedded into the concrete section. A perfect bond condition was assumed between the reinforcement bars and concrete. The constraints were applied between the steel beam and the concrete slab in order to provide full connection by constraining all rotational and translational degrees of freedoms of the nodes at the interface. Both the slab and steel beam parts within the constrained areas were meshed with similar sizes. In this case, the concrete surface acted as a master, while the steel part was assumed as a slave surface. The specimen models were constructed in full in order to enable a detailed representation of all potential instabilities, such as distortional buckling under hogging moments.

In order to determine an optimal mesh size, a number of buckling and monotonic mesh sensitivity analyses were carried out. Buckling analysis was considered in the mesh sensitivity assessment since the mesh size has a notable effect on capturing local buckling, which is critical for characterising degradation effects in steel components. While a fine mesh was used for potential plastic regions including the beam ends near the column faces and panel zones, a coarser mesh was implemented in other regions. Examples of the final 3D-FE models and mesh arrangements are illustrated in Fig. 7. Geometric imperfections were also introduced to account for typical local manufacturing tolerances. To this end, buckling analyses were carried out prior to the main analyses, and superimposition of the most critical buckling modes, such as that shown in Fig. 8, were applied by scaling within typical manufacturing tolerance levels [52].

Steel members were assigned a combined nonlinear material model from the ABAQUS material library that accounts for isotropic/kinematic hardening of the material based on a multiaxial plasticity model [53]. The assumed cyclic material parameters were based on available test results [54–56], in conjunction with the actual yield stress reported in the experimental studies. For the reinforcement, an isotropic bilinear material model with strain hardening, as suggested in EC2 [57], was employed.

The concrete damage plasticity (CDP) model [58,59] was utilised for modelling the inelastic behaviour of concrete. CDP uses the concept of isotropic damaged elasticity with isotropic tensile and compressive

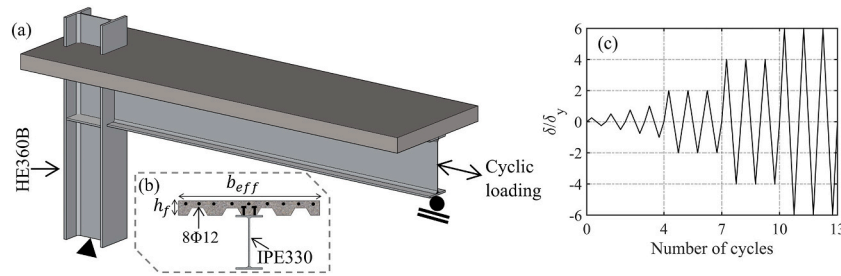


Fig. 3. Schematic test details of CS1 [47]: a) test configuration, b) composite beam cross-section, and c) applied loading history.

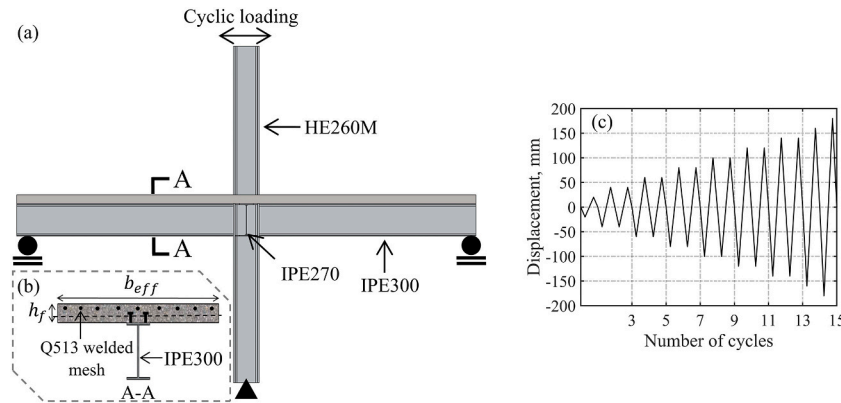


Fig. 4. Schematic test details of CS2 [48]: a) test configuration, b) composite beam cross-section, and c) applied loading history.

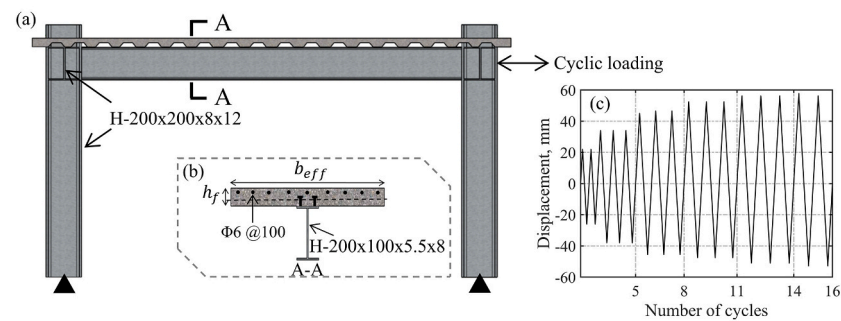


Fig. 5. Schematic test details of CS3 [49]: a) test configuration, b) composite beam cross-section, and c) applied loading history.

plasticity to simulate the inelastic behaviour of concrete. In this study, the compressive behaviour of concrete was defined as in EC2 [57] in the stress-strain domain, while the tensile behaviour of concrete was based on the CEB/FIB model code [60] in the stress-strain,  $\sigma - \epsilon$ , domain in the elastic region and the stress-crack opening,  $\sigma - \omega$ , in the plastic region, as indicated in Fig. 9a and b, respectively.

Other parameters for CDP such as the dilatation angle, eccentricity, the ratio of bi-axial-to-uniaxial compressive strength through the K parameter, and viscosity, were assumed as the default values given in ABAQUS, supported by sensitivity analysis based on combining accuracy of results and computational efficiency. The stiffness recovery factors for compression and tension were taken as 1 and 0, respectively. The damage parameters required in order to simulate the stiffness degradation of concrete were obtained from Eq. (1) as follows:

$$d = 1 - \sigma_f / f \tag{1}$$

where  $f$  is the maximum tensile or compressive strength, as appropriate. It is also assumed that no stiffness degradation occurs before the peak is reached in both the tensile and compressive parts.

### 2.3. Comparative results

Validations of the FE model were firstly performed for bare steel specimens (BS1-BS4) as discussed above. The moment at the column face versus chord rotation cyclic responses, envelope curves and deformed shapes of the specimens were compared against the test results, as shown in Fig. 10a to 10d. As shown in the figures, the numerical results are in close agreement in terms of stiffness and capacity, as well as overall cyclic behaviour. In all cases, the stiffness and capacity were captured within 2–5% of the test results. The results also show that the proposed continuum model is capable of simulating closely the hysteretic behaviour of the specimens. In addition, the ability of the 3D-FE model to simulate the local instabilities observed during the tests is also illustrated in Fig. 10. The deformation patterns from the FE results match closely the local buckling behaviour of the beam flange, which is the primary source for degradation and fracture [61], as well as any plasticity occurring within the panel zone.

After gaining confidence in the ability of the models to predict the cyclic response of bare steel specimens, validation studies were then performed for the composite specimens described previously. Fig. 11

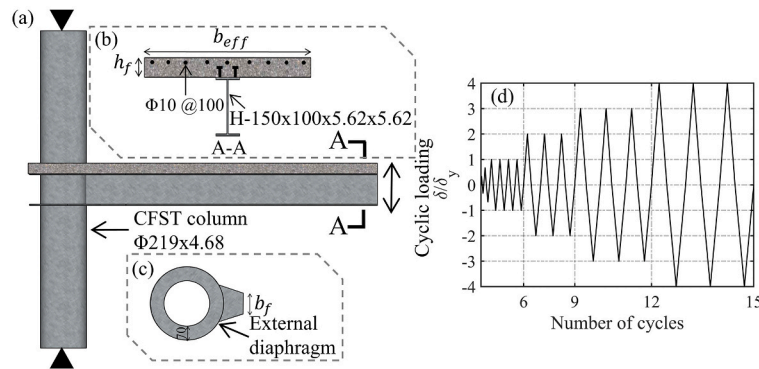


Fig. 6. Schematic test details of CS4 [50]: a) test configuration, b) composite beam cross-section, c) connection details, and d) applied loading history.

shows the comparison between the experimental and numerical results for the composite specimens. As in the case of the bare steel specimens, linear buckling analysis was firstly performed, and the critical buckling modes were superimposed and applied to the model in order to account for geometric imperfections.

For CS1, boundary conditions were assumed as a pinned support at the bottom point of the column and roller support at the loading point. The cyclic displacement loading history [51] was applied in the sliding direction (Z direction) to match that from the test. The response of Specimen CS1 is depicted in Fig. 11a and shows good agreement between the experimental results and numerical simulation. The deformed shape with different views, from 3D-FE analysis, of CS1 at the end of the largest cycle amplitude in the loading history is depicted in Fig. 12a to 12d. Buckling in the bottom flange occurred at around 250 mm away from the column face due to the presence of a flange 250 mm long and a 12 mm thick flange stiffener. As indicated in the figure, the buckling length was approximately 500 mm. As shown in Fig. 12, the concrete slab prevented buckling of the top flange and all the buckling was concentrated in the bottom flange and the bottom side of the web. The top flange remained largely elastic, whilst yielding and cyclic hardening occurred within the bottom flange and most of the web.

As shown in Fig. 11b, the numerical results for CS2 are also in close agreement with the test in terms of the beam moment at the column face against the global rotation. The same also applies to Specimen CS3, which consists of a one-storey one-bay steel frame with a composite beam. The comparison is presented in terms of global load against displacement between the 3D-FE model and the test results as shown in Fig. 11c; where  $P$  and  $U$  are lateral force and displacements of the frame, respectively, and  $sPp$  and  $sUp$  are defined as the normalisation values for lateral force and displacements of the frame, respectively. Each value is obtained by elastic calculation of a pure steel counter-frame, assuming that both end moments of the beam reach the full plastic capacity. Fig. 11c clearly shows that the proposed 3D-FE model can simulate the influence of the slab on the global behaviour of the frame, and closely predicting the stiffness, capacity, and cyclic behavioural characteristics.

Similarly, the 3D-FE and test results for CS4, which is an external composite joint specimen consisting of a CFST column and steel beam with solid reinforced concrete slab, are compared in Fig. 11d, in terms of the moment on the column face against the chord rotation of the beam. As for the other specimens, the stiffness, capacity, and cyclic degradation trends in both the positive and negative directions are captured closely through the detailed 3D continuum FE model.

In general, for all composite beams, the large deformation behaviour was broadly similar, exhibiting local buckling of the lower flange and concrete crushing in the slab. The FE models closely captured the cyclic performance of the composite specimens in terms of stiffness, capacity and, most importantly, cyclic and in-cycle degradation trends, up to the onset of fracture, which is not incorporated within the model. Discrepancies occur once fracture develops such as in the flange of the left composite beam in Specimen CS2. Overall, as shown above, the detailed

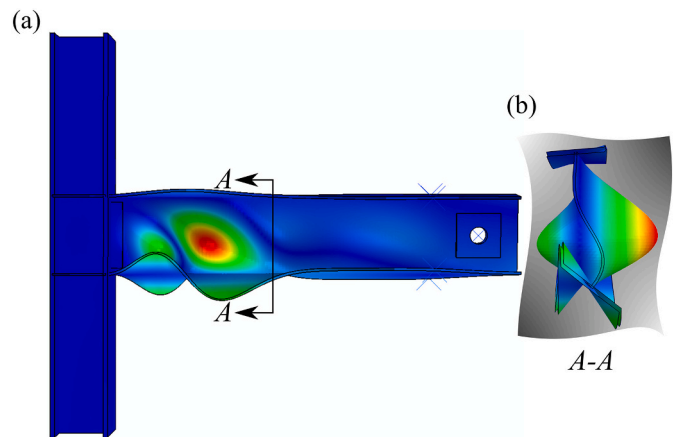


Fig. 8. Example of critical buckling mode for BS1: a) side view and b) cross-section.

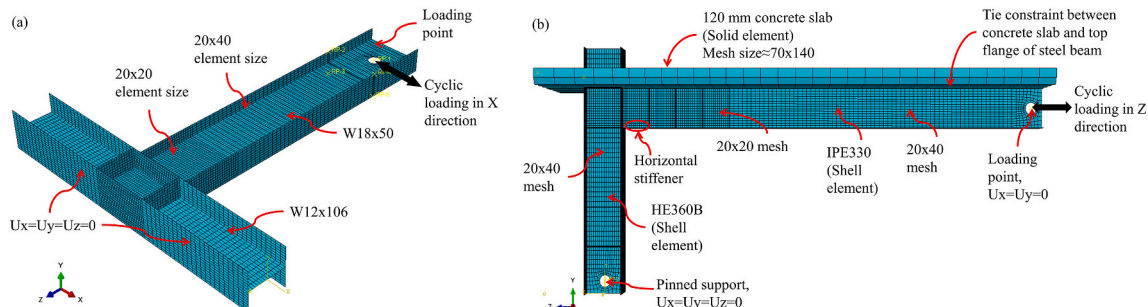


Fig. 7. Examples of continuum models: a) BS1 and b) CS1.

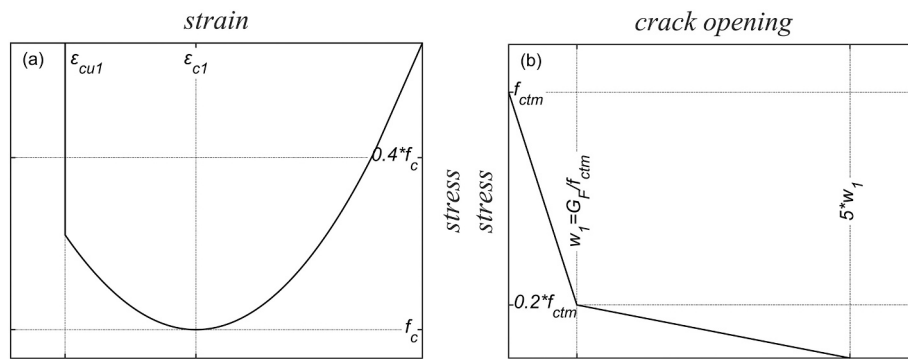


Fig. 9. Material model for concrete: (a) compression and (b) tension.

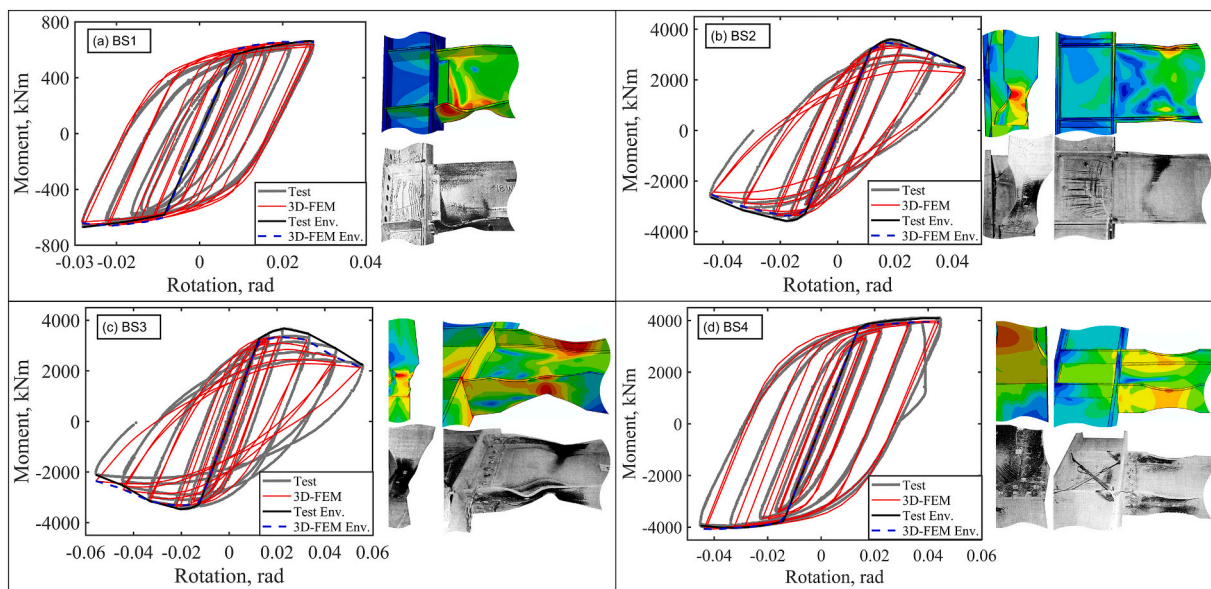


Fig. 10. Comparison between experimental and numerical results for (a) BS1, (b) BS2, (c) BS3, and (d) BS4.

continuum 3D-FE models are able to offer a faithful simulation of the behaviour, with due consideration of geometric and material nonlinearities.

The modelling approaches, which are described and validated above, provide a reliable basis for conducting parametric investigations, with a view to developing design and assessment procedures that incorporate the main cyclic deterioration effects in composite steel-concrete members, focusing on members designed to European codified provisions.

### 2.4. Parametric evaluations

The validated continuum 3D-FE modelling approach using ABAQUS [43] was utilised for conducting parametric assessments in order to generate a synthetic database for the nonlinear cyclic response of composite beams, with due account for degradation phenomena. As noted before and illustrated in Fig. 1, this synthetic database is used in the calibration of computationally efficient degradation models that can be employed in beam element representations within frame analysis. Focus was given to members designed according to European standards, using IPE and HE sections and solid slabs varying in depth from 100 mm to 200 mm. All the designed members were selected within practical geometric and material ranges and fulfilling the ductility requirements in EC8 [8] in terms of the neutral axis depth and steel section class. A list of the members and properties used in the parametric assessment is summarised in Table 3.

The composite members were modelled as idealised cantilever beams with half the length of the original span, hence replicating closely the conditions in a moment frame system. The steel beam end at the support point was fully fixed to simulate a fully welded rigid connection, whilst the concrete slab was constrained in the horizontal directions apart from the loading end to simulate slab continuity, with the bottom corner constrained vertically to avoid unrealistic vertical out of plane movement. As in the validation studies, the concrete slab and the steel beam were connected to each other through tie interaction, in which all corresponding surfaces were tied to prevent relative movement. The method of applying geometric imperfections and material models were the same as in the validation approach discussed earlier. A typical composite beam specimen with applied boundary conditions and cross-section is shown in Fig. 13a and b, respectively. Although the cyclic performance of members can be load-history dependant [62], the ECCS [51] cyclic loading protocol, widely considered to represent a severe upper bound seismic response, was adopted in the analysis in order to be consistent with current EC8 performance assessment procedures.

### 3. Uniaxial degradation modelling

In this part, an idealised degradation material model suitable for implementation within computationally efficient frame analysis studies is firstly discussed. Following the approach shown previously in Fig. 1, this section then describes the calibration procedure for the uniaxial

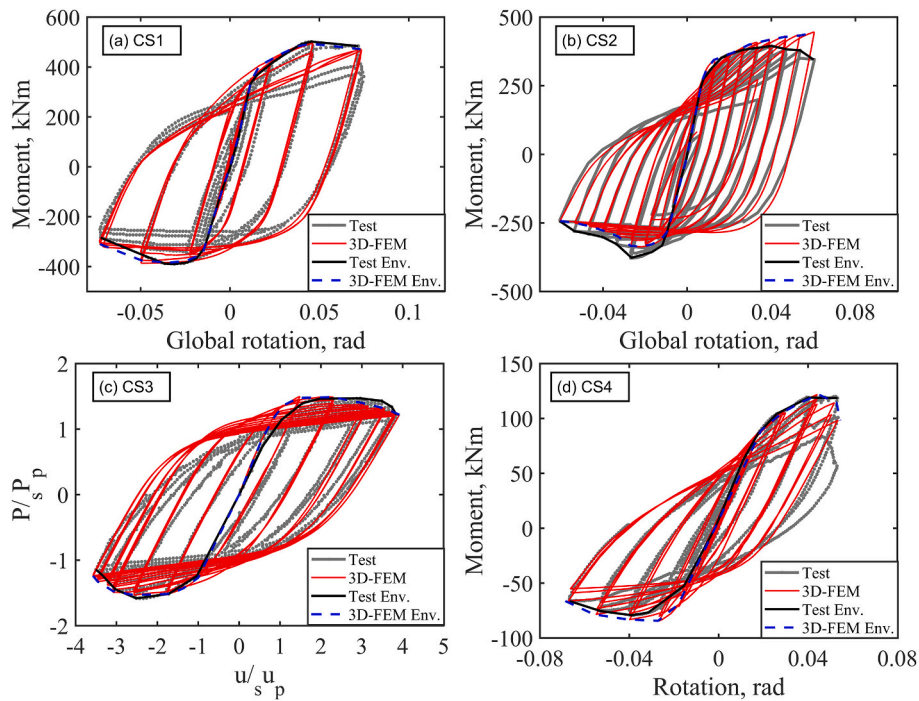


Fig. 11. Comparison between experimental and numerical results for: (a) CS1, (b) CS2, (c) CS3, (d) CS4.

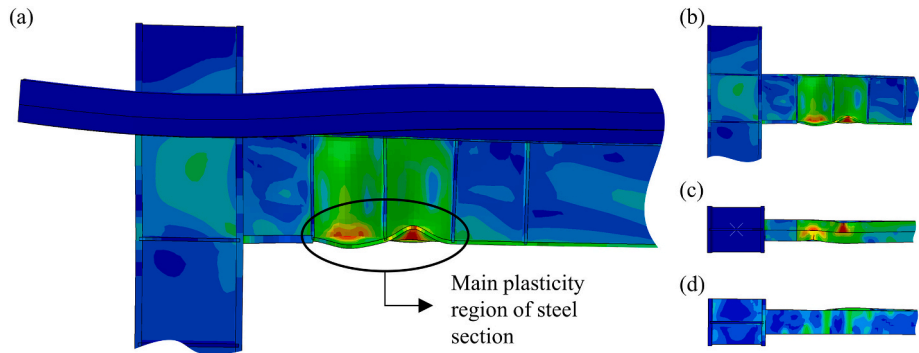


Fig. 12. Deformed shape from the analysis for Specimen CS1: a) side view of composite member, b) side view of steel component, c) bottom view of steel component, and d) top view of steel part.

degradation model using the results of the parametric studies employing the continuum 3D-FE ABAQUS models presented above.

### 3.1. Idealised material representations

The Ibarra-Medina-Krawinkler (IMK) deterioration material model [26–28] is widely used to represent cyclic degradation effects in steel components. The uniaxial model is based on a backbone curve that is similar to the monotonic behaviour of a component and defines a reference skeleton response without degradation. A set of rules are then adopted to define hysteretic behaviour, which can be applied with bilinear, peak-oriented, and pinching models, using four modes of degradation, namely: basic strength, post-capping strength, unloading stiffness, and accelerated reloading stiffness. Since the cyclic response of composite beams can be idealised closely using a bilinear hysteretic response without notable pinching, a bilinear model of the modified IMK is adopted herein. The backbone curve shown in Fig. 14 consists of the following branches: initial elastic, hardening, post-capping, and residual strength.

In the IMK material model, hysteretic energy-based rules proposed

by Rahnama and Krawinkler [63] are used to represent the cyclic degradation of structural members. Each structural element has its own energy dissipation capacity, represented by a parameter  $\Lambda$ . This is also known as the reference cumulative plastic rotation capacity, independently of the loading history, and the cyclic deterioration rates are governed by the dissipated energy in each excursion. The same rules defining the degradation in the original model [26] are employed in the latest modified version [27]. However, the original model was not able to simulate the total loss of strength as well as the asymmetric degradation which occurs in members such as composite beams. To address these limitations, Lignos [27] modified the original model by introducing a “ $D^{+/-}$ ” parameter, which defines the rate of cyclic deterioration, as discussed in subsequent sections. Other important modelling parameters are the pre-capping plastic rotation for positive/negative loading direction, often denoted as the plastic rotation capacity ( $\theta_p^{+/-}$ ), post-capping rotation for positive/negative loading direction ( $\theta_{pc}^{+/-}$ ), initial equivalent stiffness ( $K_{eq}$ ), and yield strength for sagging/hogging bending ( $M_y^{+/-}$ ) as shown in Fig. 14.

**Table 3**  
Summary of parametric assessments.

	Steel section	Investigation	$h_f$ , mm	$L$ , mm	$h_w$ , mm	$d/t_w$	$c/t_f$	$f_c$ , MPa	$f_y$ , MPa	$\rho$
Slab thickness	IPE200 to IPE500	HF100-L3-C30-S355								0.0168
		HF120-L3-C30-S355								0.013
		HF140-L3-C30-S355								0.0107
		HF150-L3-C30-S355								0.0098
		HF160-L3-C30-S355								0.009
		HF180-L3-C30-S355								0.0078
		HF200-L3-C30-S355	<b>100 to 200</b>	3000	200 to 500	28.393 to 41.765	4.14 to 5.27	30	355	0.0069
		HF150-L3-C20-S355						<b>20</b>		
		HF150-L3-C25-S355						<b>25</b>		
		HF150-L3-C30-S355						<b>30</b>		
Concrete strength	IPE300, IPE450, IPE500	HF150-L3-C30-S355	150	3000	300 to 500	35.014 to 41.765	4.61 to 5.27	<b>40</b>	355	0.0098
		HF150-L3-C30-S235						30	<b>235</b>	
		HF150-L3-C30-S355						30	<b>355</b>	
		HF150-L3-C30-S420						30	<b>420</b>	
Steel yield strength	IPE300, IPE450, IPE500	HF150-L2-C30-S355	150	3000	300 to 500	35.014 to 41.765	4.61 to 5.27	30	<b>420</b>	0.0098
		HF150-L3-C30-S355								<b>2000</b>
		HF150-L3-C30-S355								<b>3000</b>
		HF150-L4-C30-S355								<b>4000</b>
Length of the beam	IPE300, IPE360, IPE450, IPE500	HF150-L5-C30-S355	150	<b>5000</b>	300 to 500	35.014 to 41.765	4.61 to 5.27	30	355	0.0098
		HF150-L3-C30-S355- $\rho$								<b>0.006</b>
		HF150-L3-C30-S355- $\rho$								<b>0.007</b>
		HF150-L3-C30-S355- $\rho$								<b>0.01</b>
		HF150-L3-C30-S355- $\rho$								<b>0.012</b>
Rebar ratio	IPE300, IPE450, IPE500	HF150-L3-C30-S355- $\rho$	150	3000	300 to 500	35.014 to 41.765	4.61 to 5.27	30	355	<b>0.015</b>
		HF150-L3-C30-S355								
		HF150-L3-C30-S355								
Additional HE sections	HE200A to 400A HE200B to 500B HE300M to 450 M	HF150-L3-C30-S355	150	3000	200 to 500	9.90 to 27.09	2.90 to 7.88	30	355	0.0098

Bold letters depict variables in the parametric investigation.

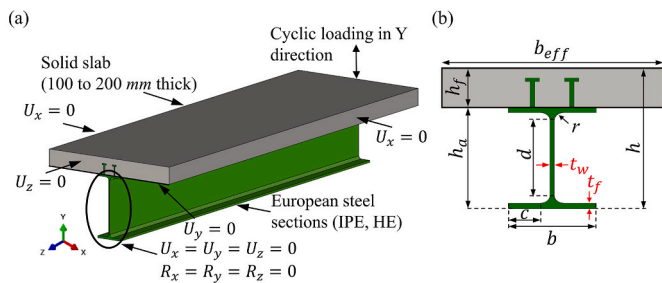


**Fig. 13.** Schematic view of parametric investigation: a) typical composite specimen and b) cross-section.

### 3.2. Calibration of IMK material model

This section describes the calibration process of the IMK model and related modelling parameters. The main purpose of this 2D-FE (uniaxial) material model calibration is to achieve a more efficient and practical modelling approach for full frame analysis since the 3D-FE (continuum) models would be computationally prohibitive. Therefore, the aforementioned ‘element-level’ 3D-FE parametric analysis was carried out to develop a wide database for calibration of the 2D-FE cyclic degradation model, according to the overall methodology described in Fig. 1.

The same 3D continuum FE cantilever composite beam members that were modelled using ABAQUS [43] for the generation of the database were also simulated using the 2D lumped plasticity approach in the nonlinear analysis program OpenSees [64]. The lumped plasticity

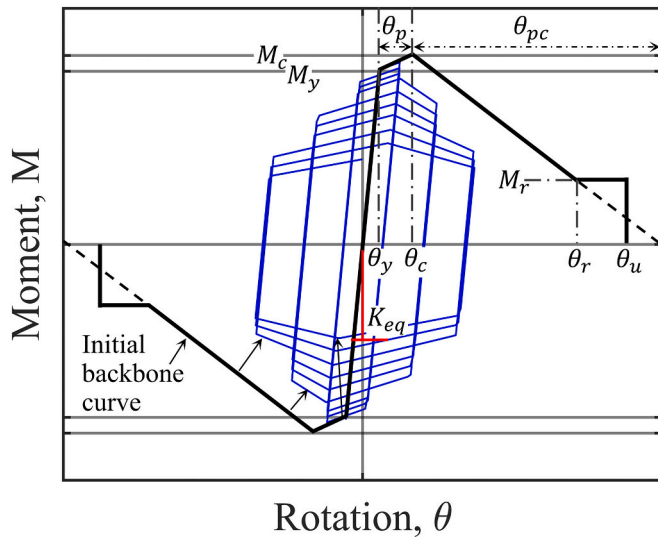


Fig. 14. Modified IMK cyclic degradation model and initial backbone curve.

model, shown in Fig. 15, comprises two elastic beam-column elements (Elements 1 and 2) connected to each other through a zero-length rotational spring (Element 3) where all the plasticity is concentrated. The elastic composite members are represented with an equivalent steel cross-section area,  $A_{eq}$ , and equivalent moment of inertia,  $I_{eq}$ , while the IMK deterioration model with bilinear hysteretic response is assigned to the rotational spring. The nonlinear behaviour of the rotational spring utilises a phenomenological material model, which simulates the cyclic deterioration in flexural strength and stiffness of the steel beam when subjected to cyclic loading. Equivalent properties were calculated with a modular ratio,  $n$ , of 7 as suggested in EC8 [8].

Previous experimental and numerical studies on steel and composite members [e.g., [65,66], as well as the detailed continuum 3D-FE studies undertaken in this investigation, have shown that the length of plastic hinge region at the beam-ends is comparable to the depth of the section. This assumption is therefore typically used in lumped plasticity models [e.g., 40] and offers reliable representation of the response when compared to tests and detailed models. Accordingly, the plastic spring is placed at half the expected plastic hinge length assumed as the section depth,  $h$ , away from the fixed support.

Within the zero-length rotational spring, the modified IMK [27] deterioration material model, which can represent the asymmetric cyclic behaviour in the presence of a concrete slab, was employed to simulate the inelastic behaviour of the composite members. The generated 3D-FE continuum synthetic database was utilised to calibrate the material model parameters simulating the cyclic moment-rotation behaviour of plastic regions in steel/concrete composite members. For this purpose, the backbone curve for both sagging and hogging bending was firstly obtained from monotonic analysis.

The initial effective stiffness  $K_{eq}$  and yield moment  $M_y^{+/-}$  values were calculated analytically according to EC4 [32] provisions. The ratio of

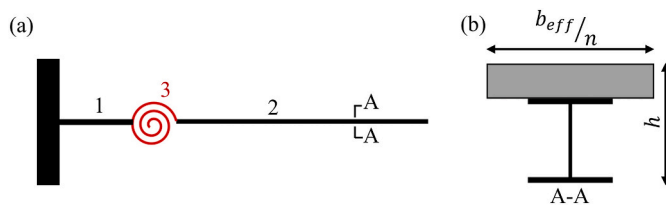


Fig. 15. 2D-FE lumped plasticity model: a) typical 2D composite specimen and b) cross-section - Elements 1 and 2: elastic beam-column; Element 3: rotational spring.

capping-to-yield strength  $(M_c/M_y)^{+/-}$ , ultimate rotation capacity  $\theta_u^{+/-}$  and residual strength  $M_r^{+/-}$  values, as suggested in previous studies [25,28], were initially considered. Following the determination of the initial backbone curve, an automated calibration process for composite members was performed to determine the deterioration parameter,  $\Lambda$ , and the parameter defining the rate of degradation for asymmetric hysteresis,  $D^+$ . The calibration process was automated to find the best combination between these deterioration parameters, by assessing the lowest normalised root mean square error (NRMSE) between the 3D-FE and 2D-FE results. The final NRMSE values for the entire database are shown in Fig. 16 with an average error of about 7%. Typical examples of the calibration plots for the modified IMK degradation model are depicted in Fig. 17.

The calibrated 2D composite IMK model described above is used in the following section to illustrate the influence of key geometric and performance parameters on the cyclic behaviour of composite members. As described in Fig. 1, these results are then subsequently used through regression assessments to produce simplified expressions which are suitable for implementation in nonlinear inelastic frame analysis of structural systems, as well as for providing information required for idealised pushover representations.

#### 4. Cyclic behavioural characteristics

This section illustrates the dependence of key modelling parameters ( $\theta_p^{+/-}$ ,  $\theta_{pc}^{+/-}$ , and  $\Lambda$ ) on the main geometric and response properties of composite members, using the calibrated composite IMK model. The scatter points for each configuration were extracted from the idealised IMK OpenSees (2D-FE) material model. The trends are illustrated by individual scatter plots of a single model parameter against a related parameter through a linear regression line. The information presented in the plots is obtained from calibrations in which the parameters of the modified IMK deterioration model are matched to the moment-rotation relationships of the steel/concrete composite beam database which was synthetically generated from the 3D continuum FE models. The regression lines are used herein for illustrating the dependency trends. On the other hand, the development of multivariate nonlinear regression equations for these modelling parameters is discussed in Section 5 below.

##### 4.1. Influence of web and flange slenderness

The influence of the web slenderness ( $d/t_w$ ), as shown in Fig. 18, is found to be significant for the behaviour in both the sagging and hogging directions. Sections with relatively slender webs are more susceptible to web local buckling under reversed loading. This encourages the buckling of lower flanges and accordingly distortional buckling. This parameter is also important for determining the cross-section classification, i.e. Class 1 to 4 according to EC3 [31].

Another important parameter used for the cross-section classification of steel sections is the flange slenderness ( $c/t_f$ ). Fig. 19 shows the dependency of modelling parameters on the flange slenderness. Whilst clear dependency is not evident when the entire database is considered, the trends become more visible for wide flange HE sections. Larger web slenderness and smaller radius of gyration ( $i_x$ ) increase susceptibility to local web buckling and distortional buckling, resulting in lower rotational capacities and higher deterioration [28]. This decreasing trend can clearly be seen in Fig. 19a, b, and c, with the pre-peak rotation and degradation being higher for low values of flange slenderness, and decreases with increasing slenderness, which is in accordance with the observations made by Araújo, et al. [67].

##### 4.2. Influence of slab thickness and steel beam depth

The thickness of the reinforced concrete slab ( $h_f$ ) and the depth of the

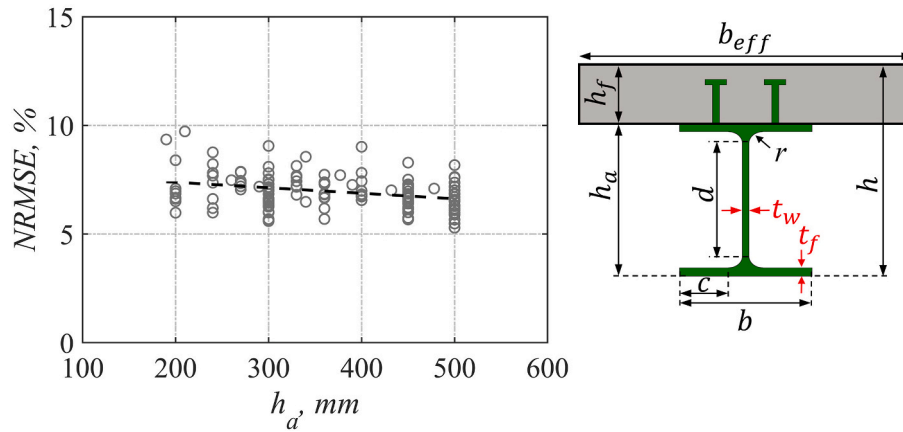


Fig. 16. Normalised root-mean-square error (NRMSE) versus steel section depth ( $h_a$ ).

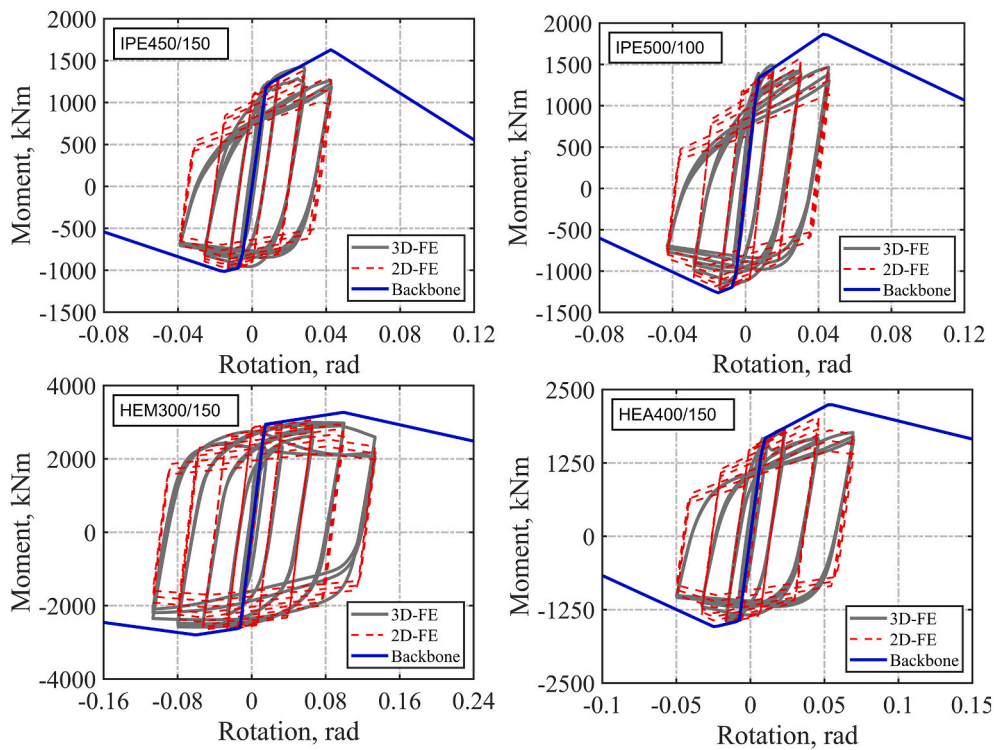


Fig. 17. Examples of IMK model calibration (initial backbone curve from 2D-FE model).

steel beam ( $h_a$ ) are two key parameters that have a direct influence on the hysteretic performance of composite members. To investigate this effect, the pre and post capping rotations ( $\theta_p^{+/-}$ ,  $\theta_{pc}^{+/-}$ ) as well as the reference energy dissipation capacity ( $\Lambda$ ), are plotted against the slab thickness and depth of the structural steel section in Figs. 20 and 21, respectively. A decreasing trend is observed in the positive rotation with the increase in the slab thickness, while the negative rotations are largely insensitive to  $h_f$  variations for both  $\theta_p$  and  $\theta_{pc}$ .  $\Lambda$  also decreases as  $h_f$  increases, which indicates more cyclic deterioration. This means that composite beams under sagging loading become less ductile when the slab thickness increases. More importantly, the depth of the steel beam has a notable effect on the cyclic response of composite beams as indicated in Fig. 21. Deeper steel beams are more prone to local buckling, hence smaller rotation capacities and less energy dissipation capacities are also expected [28]. Consequently, these two parameters are combined and represented as a ratio, i.e. ( $h_f/h_a$ ), in the regression

assessments discussed in Section 5 below.

#### 4.3. Rate of degradation

Due to the presence of the concrete slab, the cyclic response of composite beams is asymmetric, unlike bare steel counterparts which behave symmetrically under reversed loading. In order to account for this non-symmetric behaviour of composite members, Lignos [27] proposed a parameter ( $D^{+/-}$ ) that defines the rate of cyclic degradation in strength and stiffness under sagging and hogging loading. This parameter for both positive and negative directions can be assumed as 1.0 for bare steel members, while different values are considered for composite beams. In this paper, the calibration was performed by keeping  $D^-$  equal to 1.0 and changing  $D^+$  in order to obtain the best match between the results from the continuum model and the IMK model. The final  $D^+$  values are plotted against the depth of the steel beam in Fig. 22.

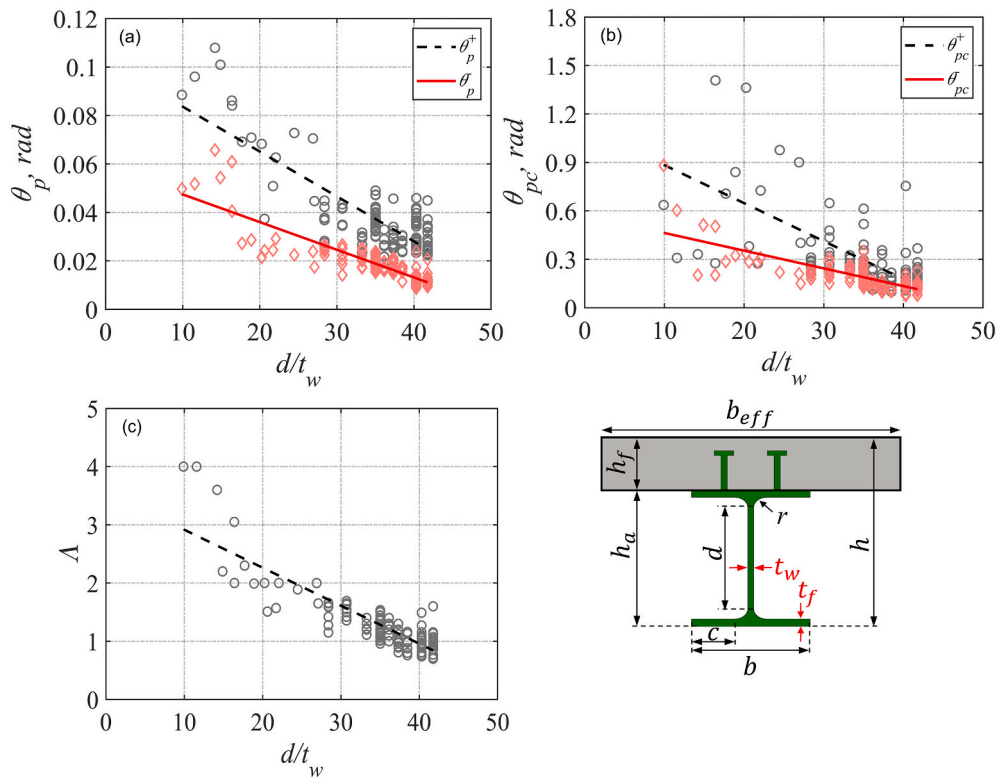


Fig. 18. Dependency of modelling parameters on web slenderness,  $d/t_w$ : a)  $\theta_p^+$ , b)  $\theta_{pc}^+$ , c)  $\Lambda$ .

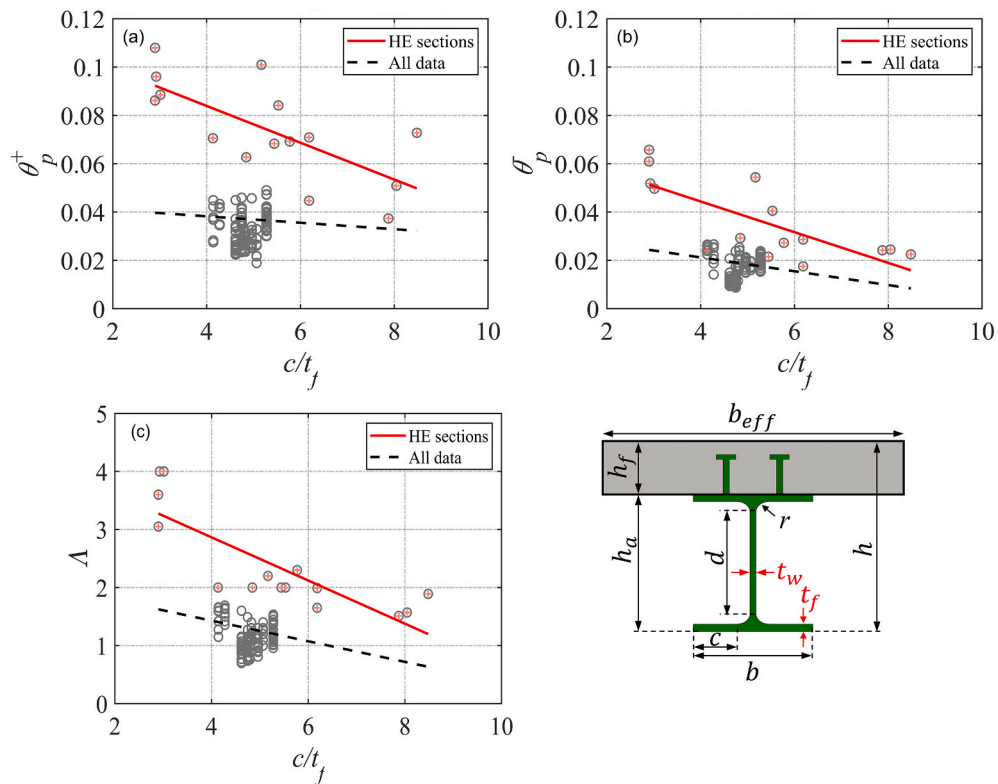


Fig. 19. Dependency of modelling parameters on flange slenderness,  $c/t_f$ : a)  $\theta_p^+$ , b)  $\theta_p^-$ , c)  $\Lambda$ .

According to the obtained results,  $D^+$  is not highly sensitive to the change in steel beam depth and is equal to 1.5 on average. Although this parameter was proposed as 1.15 in [25], this was derived from a

database which mainly consisted of composite members either without shear studs at the dissipative region or with partial interaction, which resulted in largely symmetric cyclic behaviour. Therefore,  $D^+$  is

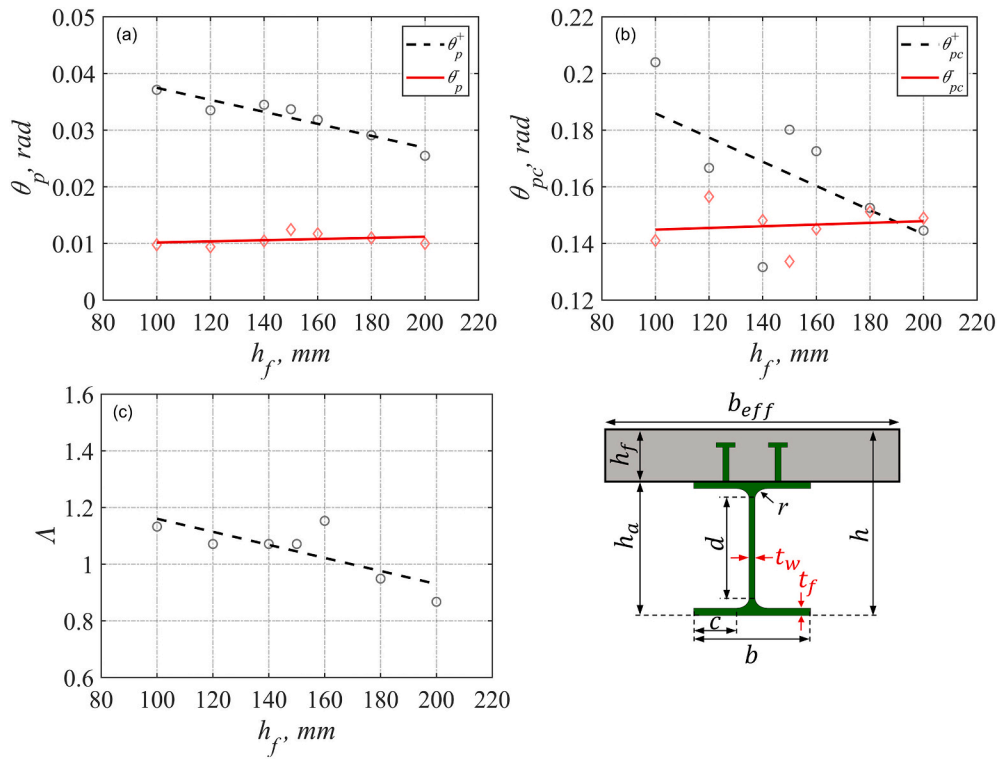


Fig. 20. Dependency of modelling parameters on slab thickness,  $h_f$  for IPE500: a)  $\theta_p$ , b)  $\theta_{pc}$ , c)  $\Lambda$ .

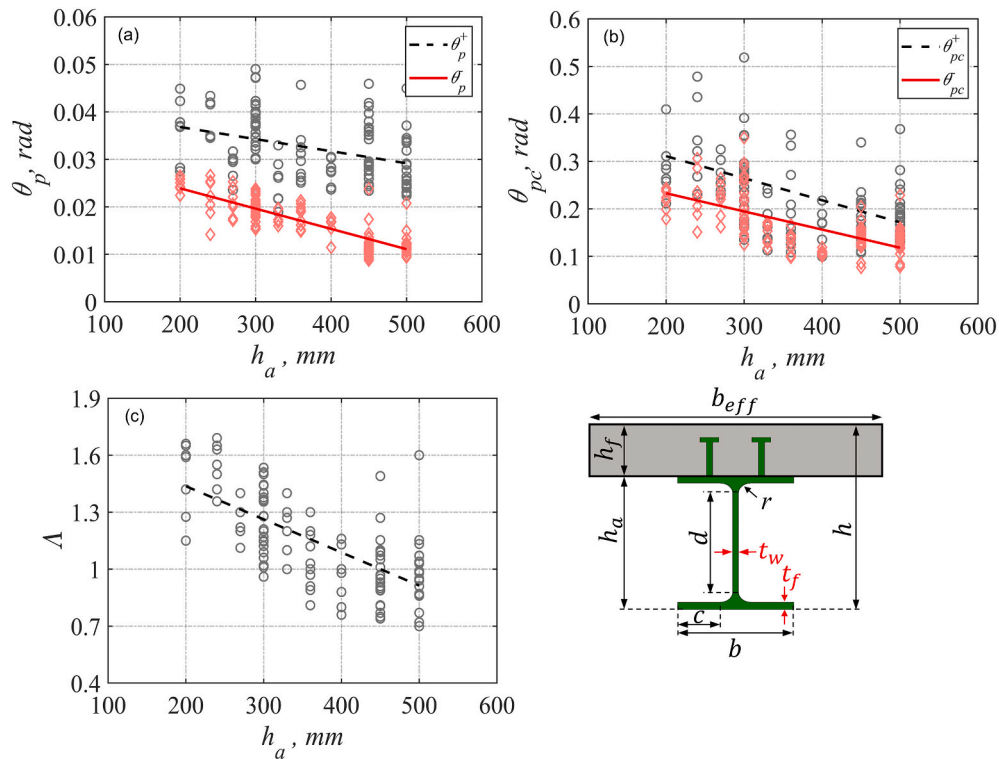


Fig. 21. Dependency of modelling parameters on steel beam depth,  $h_a$ : a)  $\theta_p$ , b)  $\theta_{pc}$ , c)  $\Lambda$ .

considered herein as 1.5 for composite beams with full connection. This affects the cyclic degradation and, therefore, the ductility under sagging bending decreases when higher values of  $D^+$  are considered, although the initial yield strength and response under hogging bending are unaffected.

#### 4.4. Normalised moment capacities

According to a recent study conducted by El Jisr, et al. [29], based on available experimental results mostly on relatively deep members used in North American practice, the plastic moment resistance of composite

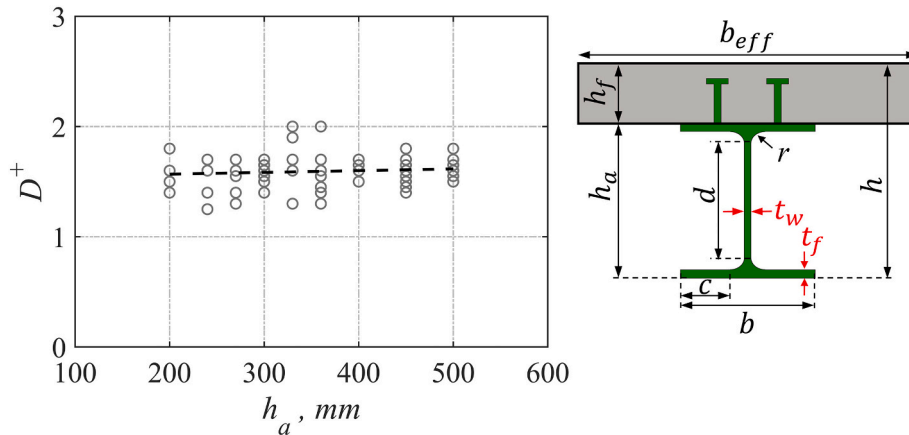


Fig. 22. Rate of cyclic degradation vs steel beam depth.

beams under positive bending is mainly dependent on the steel section depth ( $h_a$ ), span to steel beam depth ratio ( $L/h_a$ ), and the level of shear interaction between the concrete slab and steel beam, irrespective of other variations. As shown in Fig. 23, which depicts the resistance ( $M_y^+$ ) under positive loading normalised by the yield strength of the corresponding bare steel beams ( $M_{y, steel}$ ) versus  $h_a$  and the  $h_f/h_a$  ratio, the slab thickness plays an important role in the positive bending resistance of composite members. Fig. 23a shows that the concrete slab amplifies the positive bending resistance of composite beams by 50% compared to that of bare steel for deep sections ( $h_a > 400 \text{ mm}$ ), which is consistent with prior findings [5]. This amplification becomes more evident for shallower sections as the composite beam resistance can reach up to triple the steel beam resistance. On the other hand, the positive bending resistance is largely proportional to the slab thickness especially for shallow sections. As the thickness of composite beams approaches the steel section depth, the amplification increases significantly (see Fig. 23b).

Fig. 24 shows that the ratio of negative bending resistance (normalised by the plastic resistance of the bare steel section) with respect to the steel beam depth and the ratio of the entire resistance of longitudinal reinforcement to the yield resistance of the structural steel section. The resistance under negative loading is shown to be proportional to the steel section depth and the amount of reinforcement within the effective width especially for shallow sections. The plastic resistance of composite beams under negative bending is increased by 10–50% compared to the bare steel section yield strength, depending on the depth of the steel beam as shown in Fig. 24a. Whilst deeper sections ( $h_a > 400 \text{ mm}$ ) experience less amplification, as also noted in previous studies [25,29], the increase in the negative bending resistance of shallower sections is more pronounced as observed in previous tests [5,47]. As evident from Fig. 24b, the amount of reinforcement has a significant effect on the

plastic resistance under hogging bending.

On the other hand, post-yield hardening is described as the ratio of capping moment in the backbone curve,  $M_c$ , to the yield strength of the member,  $M_y$  [28]. This ratio together with  $\theta_c/\theta_y$  define the hardening of the backbone curve shown in Fig. 14. Post-yield hardening values for both positive and negative loading are relatively stable with values of 1.3 and 1.1, respectively, as shown in Fig. 25a and b. These are consistent with the suggested values proposed for the imminent second generation of EC8 [68].

#### 4.5. Equivalent stiffness

The initial equivalent stiffness of composite members, normalised to that of the bare steel beam, is depicted in Fig. 26a and b with respect to the steel beam depth and the ratio of slab thickness to steel beam depth, respectively. The composite action at least doubles the stiffness for deep sections within the database ( $h_a > 400 \text{ mm}$ ). This is in agreement with previous test results [5], which concluded that composite action nearly doubles the flexural stiffness compared to bare steel counterparts with 400 mm depth. This amplification is even more significant for shallower sections.

As indicated in Fig. 26b, the concrete slab thickness has a significant influence on the equivalent stiffness of composite members. The equivalent stiffness of composite beams is proportional to the ratio of slab thickness to steel beam depth. The effective stiffness is also dependent on the level of shear interaction between the concrete slab and the steel beam [29], yet this is not taken into account herein since partial interaction is effectively not permitted for dissipative design in EC8 [8], as discussed in earlier sections.

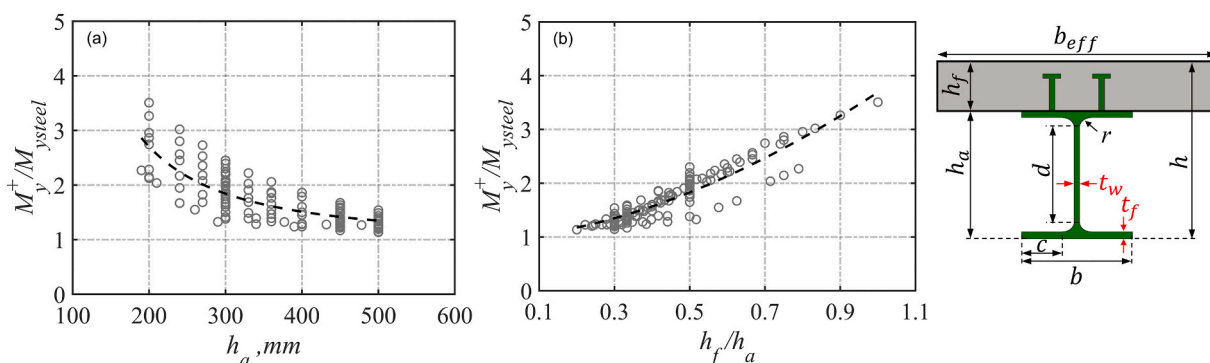


Fig. 23. Ratio of yield strength of composite beam to that of steel beam under positive bending vs: a)  $h_a$  and b)  $h_f/h_a$ .

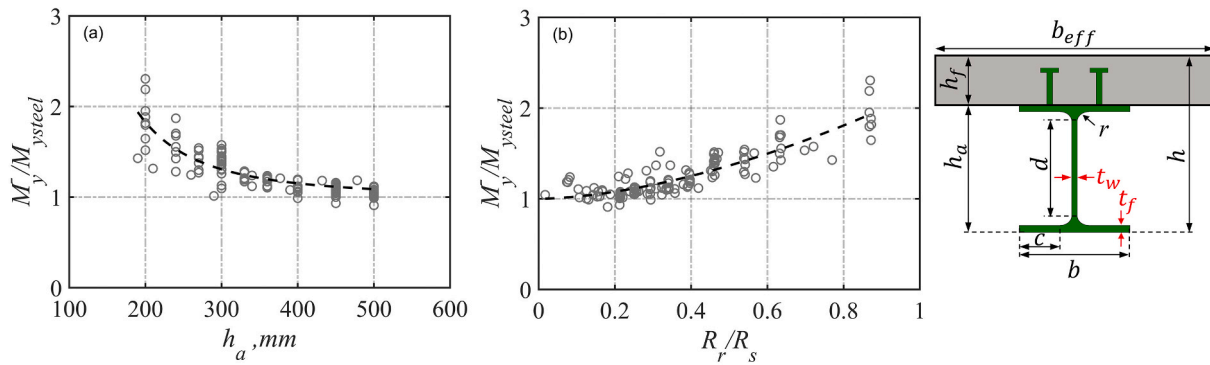


Fig. 24. Ratio of yield strength of composite beam to that of steel beam under negative bending vs: a)  $h_a$  and b)  $R_r/R_s$ .

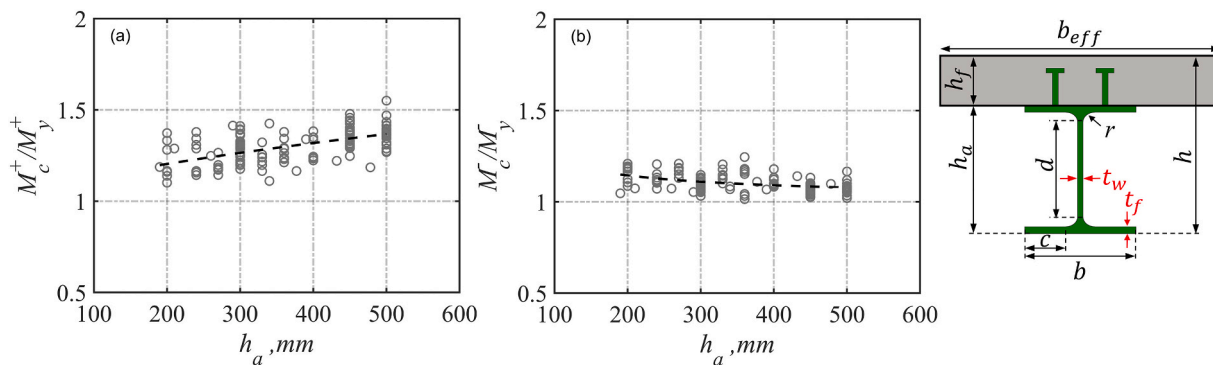


Fig. 25. Ratio of ultimate strength of composite beam to its yield strength for: a) positive and b) negative bending.

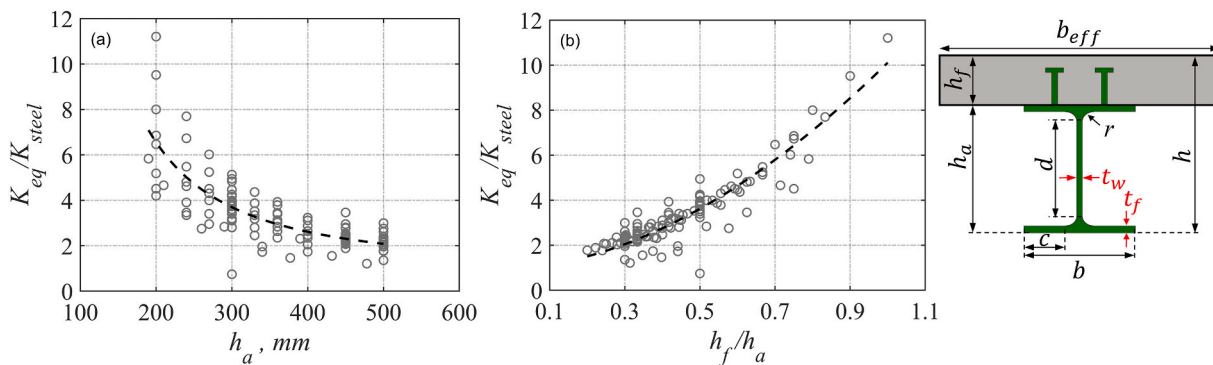


Fig. 26. Equivalent initial stiffness of composite members normalised by that of bare steel beams vs: a)  $h_a$  and b)  $h_f/h_a$ .

## 5. Proposed degradation relationships

### 5.1. Regression expressions

A multivariable nonlinear regression relationship, given in Eq. 2, was used to model and assess the cyclic behaviour and the deterioration of composite members consisting of steel beams with fully connected reinforced concrete slabs. The parameters governing the relationships are identified using the results presented in this paper coupled with information available from previous studies [28,67,69].

A parameter pool, depending on geometric and material properties of the members, was firstly prepared, and the influence of each parameter on the cyclic response, including degradation, was investigated separately. Additionally, the accuracy and practicality of the generated regression equations were evaluated by checking  $R^2$  values, and the statistical significance of each parameter was also assessed.

Parameters with high  $p$ -values ( $\geq 5\%$ ) of low influence on the accuracy of the regression were considered as statistically insignificant. All considered parameters, namely the web and flange slenderness of structural steel ( $d/t_w$ ,  $c/t_f$ ); ratio of  $L_b$  (defined as the distance between support point, or column face, and the nearest lateral brace) to  $i_z$  (defined as the radius of gyration about the weak axis of structural steel) (i.e.  $L_b/i_z$ ); ratio of length of composite beam to depth of steel section ( $L/h_a$ ); ratio of yield strength of steel to characteristic compressive strength of concrete ( $f_{yd}/f_{ck}$ ); ratio of thickness of concrete slab to depth of structural steel and composite sections ( $h_f/h_a$ ,  $h_f/h$ ); ratio of cross-sectional area of concrete slab to the area of structural steel ( $A_c/A_s$ ); and ratio of total strength of the reinforcement bars within the effective width to the axial strength of structural steel ( $R_r/R_s$ ), are included in the general regression presented by Eq. 3.  $L_b/i_z$  was found to be insignificant in the quantification of degradation parameter, which is in agreement with previous findings [70].

$$Y = c_1 \cdot X_1^{c_2} \cdot X_2^{c_3} \cdot X_3^{c_4} \dots X_n^{c_{n+1}} \quad (2)$$

composite beam sections within the data range given above could be plotted for practical design and assessment purposes. Fig. 27 illustrates the backbone curves for two selected structural steel sections, IPE200

$$Y = c_1 \cdot \left(\frac{d}{t_w}\right)^{c_2} \cdot \left(\frac{c}{t_f}\right)^{c_3} \cdot \left(\frac{L_b}{i_z}\right)^{c_4} \cdot \left(\frac{L}{h_a}\right)^{c_5} \cdot \left(\frac{f_{yd}}{f_{ck}}\right)^{c_6} \cdot \left(\frac{h_f}{h}\right)^{c_7} \cdot \left(\frac{A_c}{A_s}\right)^{c_8} \cdot \left(\frac{R_r}{R_s}\right)^{c_9} \quad (3)$$

Based on the regression assessments, the relationships presented below can be derived.

Pre-capping plastic rotation for positive and negative bending:

$$\theta_p^+ = 0.26461 \cdot \left(\frac{d}{t_w}\right)^{0.78606} \cdot \left(\frac{c}{t_f}\right)^{-1.4035} \cdot \left(\frac{L_b}{i_z}\right)^{-1.8592} \cdot \left(\frac{L}{h_a}\right)^{2.1684} \cdot \left(\frac{f_{yd}}{f_{ck}}\right)^{-0.46107} \cdot \left(\frac{h_f}{h}\right)^{-0.58095} \quad (R^2 = 0.812) \quad (4)$$

$$\theta_p^- = 0.97286 \cdot \left(\frac{d}{t_w}\right)^{1.2109} \cdot \left(\frac{c}{t_f}\right)^{-2.3412} \cdot \left(\frac{L_b}{i_z}\right)^{-2.1045} \cdot \left(\frac{L}{h_a}\right)^{2.2227} \cdot \left(\frac{f_{yd}}{f_{ck}}\right)^{-0.42878} \cdot \left(\frac{h_f}{h}\right)^{0.49236} \quad (R^2 = 0.827) \quad (5)$$

Post-capping rotation for positive and negative bending:

$$\theta_{pc}^+ = 2.7848 \cdot \left(\frac{d}{t_w}\right)^{4.331} \cdot \left(\frac{c}{t_f}\right)^{-1.1789} \cdot \left(\frac{L}{h_a}\right)^{4.1524} \cdot \left(\frac{f_{yd}}{f_{ck}}\right)^{-1.2949} \cdot \left(\frac{h_f}{h}\right)^{7.1177} \cdot \left(\frac{A_c}{A_s}\right)^{-4.0892} \quad (R^2 = 0.54) \quad (6)$$

$$\theta_{pc}^- = 1345 \cdot \left(\frac{d}{t_w}\right)^{-4.6568} \cdot \left(\frac{c}{t_f}\right)^{3.0382} \cdot \left(\frac{L_b}{i_z}\right)^{3.5062} \cdot \left(\frac{L}{h_a}\right)^{-3.809} \cdot \left(\frac{f_{yd}}{f_{ck}}\right)^{-0.52624} \cdot \left(\frac{h_f}{h}\right)^{0.47526} \cdot \left(\frac{R_r}{R_s}\right)^{0.067621} \quad (R^2 = 0.808) \quad (7)$$

Cyclic degradation parameter (same for all degradation modes):

$$\Lambda = 83.888 \cdot \left(\frac{d}{t_w}\right)^{-0.93834} \cdot \left(\frac{c}{t_f}\right)^{-0.26856} \cdot \left(\frac{f_{yd}}{f_{ck}}\right)^{-0.22977} \cdot \left(\frac{h_f}{h}\right)^{-0.062963} \quad (R^2 = 0.87) \quad (8)$$

Normalised moment capacities:

$$\frac{M_y^+}{M_{y,steel}} = 1.0 + 2.913 \cdot \left(\frac{h_f}{h_a}\right)^{1.2044} \cdot \left(\frac{R_r}{R_s}\right)^{0.46392} \quad (R^2 = 0.938) \quad (9)$$

$$\frac{M_y^-}{M_{y,steel}} = 1.0 + 1.5438 \cdot \left(\frac{h_f}{h_a}\right)^{1.174} \cdot \left(\frac{R_r}{R_s}\right)^{0.96757} \quad (R^2 = 0.915) \quad (10)$$

Equivalent stiffness:

$$\frac{K_{eq}}{K_{steel}} = 1.0 + 9.108 \cdot \left(\frac{h_f}{h_a}\right)^{1.798} \quad (R^2 = 0.8618) \quad (11)$$

The above equations are valid within the following data ranges:  $9.90 \leq d/t_w \leq 41.765$ ,  $2.90 \leq c/t_f \leq 8.2$ ,  $235 \text{ MPa} \leq f_{yd} \leq 420 \text{ MPa}$ ,  $100 \text{ mm} \leq h_f \leq 200 \text{ mm}$ ,  $20 \text{ MPa} \leq f_{ck} \leq 40 \text{ MPa}$ .

Using the proposed regression equations, backbone curves for the

(Fig. 27a) and IPE500 (Fig. 27b), with different slab thicknesses of 200 mm, 150 mm, and 100 mm. Fig. 27 clearly shows that an increase in the slab thickness affects the capacity and stiffness as well as the rotation properties. This influence is more pronounced in shallow sections as

indicated in Fig. 27a, with the yield strength under positive bending being between two- to four-fold the bare steel counterpart for slab thickness of 100 mm and 200 mm, respectively. For deeper sections, as

shown in Fig. 27b, the concrete slab increases the positive bending resistance of composite beams by 20% to 50% for 100 mm and 200 mm thick slab, respectively, compared to bare steel.

## 5.2. Comparative assessments

This section compares the proposed relationships to the provisions suggested in the draft revision of EC8 [68] as well as equations proposed in previous studies [28,29], in terms of the plastic rotation capacity as defined in EC8-Part 3 [33] and the cyclic degradation parameter as proposed by Lignos and Krawinkler [28].

The plastic rotation capacities, defined in Table B.1 of EC8-Part 3 [33] with respect to steel section classes for three performance limit states, namely: Damage Limitation (DL), Significant Damage (SD), and Near Collapse (NC), are  $1.0\theta_y$ ,  $6.0\theta_y$ , and  $8.0\theta_y$ , respectively, where  $\theta_y$  is the chord rotation at yield, hence for a cantilever beam  $\theta_y = M_p L / 3EI$ . In this paper, the full plastic mechanism is considered, therefore the rotation capacities at NC limit states corresponding to the plastic rotation capacity at 20% drop in the peak strength of members [71,72] are compared. This value is estimated approximately as  $\theta_p, 80\% = 8.0\theta_y$  for bare steel structural members in EC8-Part3 [33], whilst it is calculated as  $\theta_p, pred = \theta_p^{+/-} + 0.2\theta_{pc}^{+/-}$  by using the relationships proposed in this paper. El Jisr, et al. [29] also used the same approach but adopted the formulations for bare steel members without investigating cyclic degradation.

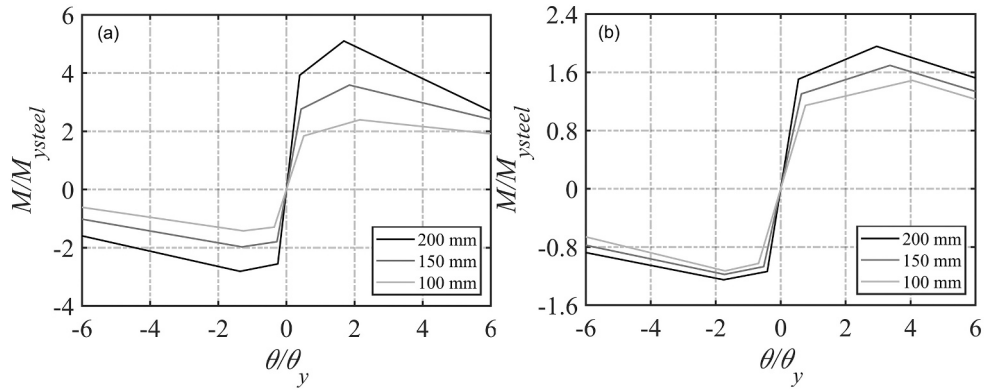


Fig. 27. Examples of backbone curves for various slab thicknesses,  $h_f$ , (as 200 mm, 150 mm, and 100 mm) plotted via proposed formulations: a) IPE200, and b) IPE500.

In order to assess the cyclic degradation of steel beams with a concrete slab,  $\Lambda_{pred}$  is calculated using the proposed formulation in this paper and normalised by the cyclic deterioration parameter,  $\Lambda$ , obtained for the entire database by the formulae proposed in [28] for bare steel members. Elkady and Lignos [25] also considered cyclic degradation in composite beams as discussed above, yet their study concluded that  $\Lambda$  was the same as in [28] for bare steel members. The normalised data for cyclic deterioration parameter is plotted in Fig. 28 versus the steel section depth.

As indicated in Fig. 28a and b, the plastic rotation capacity under positive (sagging) bending is generally higher than that under negative (hogging) loading. This is expected as the concrete slab provides lateral restraint to the top flange and the upper part of the web of the steel beam, thereby delaying or preventing local buckling under sagging loading. However, this is the opposite for the plastic rotation capacity under sagging bending. Due to the presence of the longitudinal reinforcement in the concrete slab, the plastic neutral axis is shifted

upwards, thereby causing larger strain demands on the bottom flange of the steel beam. This leads to early local buckling and subsequently fracture of the bottom part of the steel beam under reversed loading.

Fig. 28a and b show that EC8-Part 3 [33] overestimates the positive and negative plastic rotation capacities by around 30% and 50%, respectively. This is in agreement with previous studies [29,67]. The main reason for this is that EC8 does not consider the influence of geometric and material properties on the rotation capacity. As for the predictions by El Jisr, et al. [29], the positive rotation capacities are low compared to the findings from the equations proposed herein, as the formulations used are intended for bare steel members. In order to take into account of the effects of composite action on the positive rotation capacity, an amplification factor of 1.5 (already implemented in the calculations here) for plastic rotation capacity is incorporated by El Jisr, et al. [29]. This does not represent fully connected composite members, as discussed before, since the database was mostly composed of composite steel beams either with low levels of shear connection or without

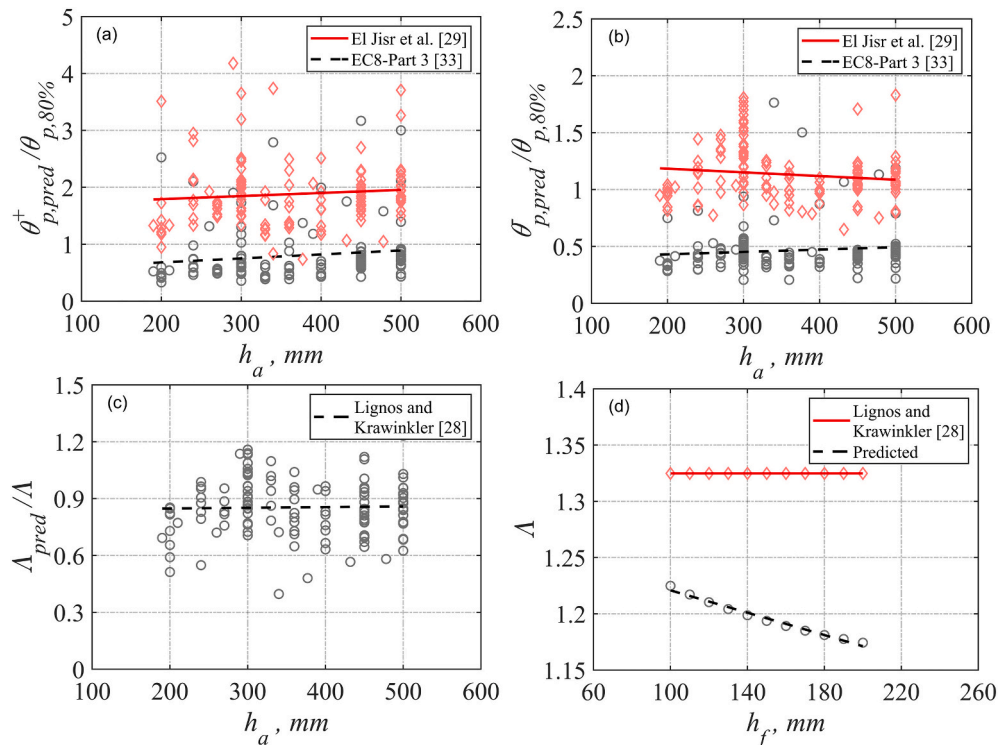


Fig. 28. Comparison of plastic rotation and cyclic deterioration parameter vs steel beam depth: a)  $\theta_p^+$ , b)  $\theta_p^-$ , c)  $\Lambda$ , as well as d) cyclic deterioration parameter for IPE300 vs slab thickness.

shear studs in dissipative zones, which is not considered as a composite section in seismic design to EC8 [8]. On the other hand, the predictions for the negative rotation capacity from this research is broadly similar, within about 10%, to the findings of El Jisr, et al. [29] for bare steel members. In particular, for deep sections ( $h_a > 400 \text{ mm}$ ), this ratio is even closer to unity, which is also in agreement with the proposed revisions of EC8 [68] since it proposes the same approach as that in El Jisr, et al. [29].

As for degradation in the cyclic behaviour of composite beams, Fig. 28c and 28d compare the proposed equations in this paper to the suggested formulations for bare steel members by Lignos and Krawinkler [28] and which are also directly used without modification in the study by Elkady and Lignos [25] for composite beam members. As indicated in the figure, the latter overestimates the energy dissipation capacity by around 20% compared to the degradation observed based on the results from this paper. This is expected as under negative bending early local buckling of the steel beam flange occurs due to the shifting upwards of the plastic neutral axis and, hence, higher strain demands occur in the bottom part of the steel beam in the presence of the slab, followed by the crushing of the concrete slab in compression under positive bending during subsequent cycles. Therefore, this leads to higher degradation in both the positive and negative loading directions. Elkady and Lignos [25] also suggested using the same value for  $\Lambda$  in composite beams as that proposed in [28] for bare steel members. However, as, discussed earlier, the experimental database used in these previous studies, apart from one test series ( $h_a \approx 460 \text{ mm}$ ), largely consisted of deep sections ( $h_a \approx 910 \text{ mm}$ ) without shear studs in the dissipative regions, which does not comply with European seismic design rules for composite beams [8,32], whilst shallower sections ( $h_a < 500 \text{ mm}$ ) with full connected composite beams are commonly adopted in European design practice. As also seen in Fig. 28d, the formulation in [28] for  $\Lambda$  is insensitive to the change in slab thickness, whilst the magnitude of degradation parameter,  $\Lambda$ , decreases as the slab thickness increases according to the predicted values calculated using the relationships proposed in this paper.

The cyclic degradation expressions for composite beams proposed in this paper enable the reliable use of uniaxial deterioration models within computationally efficient nonlinear inelastic frame analysis for structural systems. These expressions also provide fundamental information required for idealised pushover representations for practical seismic assessment and design purposes.

## 6. Concluding remarks

This paper has investigated the inelastic behaviour of composite steel concrete floor beams, with particular emphasis on cyclic deterioration effects. A continuum model was firstly developed to represent the hysteretic response of composite steel beam and concrete slab assemblages, supported by validation studies against various available experimental cyclic results on both steel and composite members. The proposed model was then adopted to perform detailed parametric assessments which were used to gain insights into the key response characteristics related to the inelastic cyclic performance of composite steel/concrete members, including their stiffness and capacity. The parametric results were subsequently used to develop relationships governing the plastic rotation and cyclic degradation of dissipative composite beams as a function of the main geometric and material properties, with focus on members designed to European codified procedures. The main findings can be summarised as follows:

- It was shown that the proposed three-dimensional continuum finite element modelling approach was able to represent the cyclic behaviour of both bare steel and composite members, capturing closely the stiffness and capacity as well as the main cyclic deterioration phenomena.
- The main deterioration modelling parameters, namely the pre- and post-capping rotation degradation (i.e.  $\theta_p^{+/-}$ ,  $\theta_{pc}^{+/-}$ ) were found to

be most significantly affected by the slenderness of the steel beam web and flange, while the beam length and depth were also shown to be key parameters that affect the cyclic response.

- The parameter  $L_b/i_z$ , describing the lateral stiffness of the steel beam, was shown to be more important under negative (hogging) bending compared to positive (sagging) bending, as expected, as the out of plane movement of the top flange of the steel beam is restrained by the concrete slab.
- The parameter that defines the asymmetric rate of cyclic degradation in strength and stiffness under sagging bending,  $D^+$ , was found on average to be around 1.5 for fully connected composite beams.
- Formulations for modelling the equivalent stiffness as well as yield strength of composite beams for both positive and negative bending were proposed, based on the cyclic response of composite members with full shear interaction. These parameters have a direct influence on the capacity design criteria as well as serviceability limits and inelastic response.
- Compared to bare steel sections, composite action increases the equivalent stiffness for deep sections ( $h_a > 400 \text{ mm}$ ) by over two-fold, and even more for shallower sections. Significant increases of around 50% and 10% also occur in the positive and negative moment capacities, respectively, for such sections. For shallower sections, these amplifications can be even higher, reaching up to three-folds for positive bending and 50% for negative bending, depending on the steel section depth, the slab thickness, and the amount of reinforcement within the effective width.
- The post yield hardening ratios of capping moment,  $M_c$ , to the yield strength  $M_y$ , were typically 1.3 and 1.1 for the positive and negative directions, respectively.
- The plastic rotation capacity under positive bending is higher than that of negative bending due to the out of plane restraint of the top flange by the concrete slab. It was shown that EC8-Part 3 overestimates this by about 30% and 50% for positive and negative bending, respectively, and does not account for the effects of geometric and material nonlinearities on the rotation capacity.
- The findings from this study regarding the cyclic degradation parameter,  $\Lambda$ , differ from prior results on bare steel sections by around 20%. This is expected due to the upward shifting of the plastic neutral axis in the presence of the slab, thereby inducing more demand on the bottom part of steel section as well as the crushing of concrete slab under positive loading, leading to lower ductility in both the positive and negative loading directions.

Overall, it was shown that the developed hysteretic relationships offer a reliable representation of cyclic degradation effects in composite structural components. The proposed expressions are suitable for implementation in nonlinear inelastic frame analysis of structural systems, as well as for providing information required for idealised pushover representations for practical seismic assessment and design.

## Declaration of Competing Interest

There are no conflicts of interest in this submission.

## Acknowledgements

The financial support provided for the first author from the Republic of Turkey Ministry of National Education to undertake his PhD studies at Imperial College London is gratefully acknowledged.

## References

- [1] A.Y. Elghazouli, J.M. Castro, Design of composite steel/concrete structures, in: A. Y. Elghazouli (Ed.), *Seismic design of buildings to Eurocode*, Second ed. 8, CRC Press, Taylor & Francis Group, 2016 ch. 7.

- [2] C.T. Cheng, C.F. Chan, L.L. Chung, Seismic behavior of steel beams and CFT column moment-resisting connections with floor slabs, *J. Constr. Steel Res.* 63 (11) (2007) 1479–1493.
- [3] M.D. Engelhardt, G. Fry, S. Jones, M. Venti, S. Holliday, Behavior and design of radius cut reduced beam section connections, *Rep. No. SAC/BD-00* vol. 17, 2000.
- [4] J.R. Liew, T. Teo, N. Shanmugam, C. Yu, Testing of steel–concrete composite connections and appraisal of results, *J. Constr. Steel Res.* 56 (2) (2000) 117–150.
- [5] M. Nakashima, T. Matsumiya, K. Suita, F. Zhou, Full-scale test of composite frame under large cyclic loading, *J. Struct. Eng.* 133 (2) (2007) 297–304.
- [6] J. Ricles, X. Zhang, J. Fisher, L. Lu, Seismic performance of deep column-to-beam welded reduced beam section moment connections, in: *Proceedings of the 5th International Workshop on Connections in Steel Structures*, Amsterdam, 2004, pp. 211–222.
- [7] AISC 358–16, *Prequalified connections for special and intermediate steel moment frames for seismic applications, including supplements* no. 1 and no. 2. (ANSI/AISC 358-16 with ANSI/AISC 358s1–18 and ANSI/AISC 358s2–20), American Institute for Steel Construction, Chicago, 2016.
- [8] EN 1998–1, Eurocode 8: Design Provisions for Earthquake Resistance of Structures, Part 1: General Rules, Seismic Actions and Rules for Buildings, European Committee for Standardization, CEN, Brussels, 2004.
- [9] Y.C. Wang, Deflection of steel-concrete composite beams with partial shear interaction, *J. Struct. Eng.* 124 (10) (1998) 1159–1165.
- [10] E. El-Lobody, D. Lam, Finite element analysis of steel-concrete composite girders, *Adv. Struct. Eng.* 6 (4) (2003) 267–281.
- [11] U. Katwal, Z. Tao, M.K. Hassan, Finite element modelling of steel-concrete composite beams with profiled steel sheeting, *J. Constr. Steel Res.* 146 (2018) 1–15.
- [12] D.J. Oehlers, N.T. Nguyen, M. Ahmed, M.A. Bradford, Partial interaction in composite steel and concrete beams with full shear connection, *J. Constr. Steel Res.* 41 (2–3) (1997) 235–248.
- [13] J. Nie, C.S. Cai, Steel–concrete composite beams considering shear slip effects, *J. Struct. Eng.* 129 (4) (2003) 495–506.
- [14] Q.Q. Liang, B. Uy, M.A. Bradford, H.R. Ronagh, Strength analysis of steel–concrete composite beams in combined bending and shear, *J. Struct. Eng.* 131 (10) (2005) 1593–1600.
- [15] F. Queiroz, P. Vellasco, D. Nethercot, Finite element modelling of composite beams with full and partial shear connection, *J. Constr. Steel Res.* 63 (4) (2007) 505–521.
- [16] J. Nie, C.S. Cai, T. Wang, Stiffness and capacity of steel–concrete composite beams with profiled sheeting, *Eng. Struct.* 27 (7) (2005) 1074–1085, <https://doi.org/10.1016/j.engstruct.2005.02.016>.
- [17] X. Liu, M.A. Bradford, Q.-J. Chen, H. Ban, Finite element modelling of steel–concrete composite beams with high-strength friction-grip bolt shear connectors, *Finite Elem. Anal. Des.* 108 (2016) 54–65.
- [18] Y. Huang, W. Yi, R. Zhang, M. Xu, Behavior and design modification of RBS moment connections with composite beams, *Eng. Struct.* 59 (2014) 39–48, <https://doi.org/10.1016/j.engstruct.2013.10.022>.
- [19] A. Rossi, R.S. Nicoletti, A.S.C. de Souza, C.H. Martins, Numerical assessment of lateral distortional buckling in steel-concrete composite beams, *J. Constr. Steel Res.* 172 (2020), <https://doi.org/10.1016/j.jcsr.2020.106192>.
- [20] O.S. Bursi, F.-F. Sun, S. Postal, Non-linear analysis of steel–concrete composite frames with full and partial shear connection subjected to seismic loads, *J. Constr. Steel Res.* 61 (1) (2005) 67–92, <https://doi.org/10.1016/j.jcsr.2004.06.002>.
- [21] J. Castro, A.Y. Elghazouli, B. Izzuddin, Modelling of the panel zone in steel and composite moment frames, *Eng. Struct.* 27 (1) (2005) 129–144.
- [22] A. Braconi, W. Salvatore, R. Tremblay, O. Bursi, Behaviour and modelling of partial-strength beam-to-column composite joints for seismic applications, *Earthq. Eng. Struct. Dyn.* 36 (1) (2007) 142–161.
- [23] J. Nie, K. Qin, C.S. Cai, Seismic behavior of connections composed of CFSSTCs and steel–concrete composite beams — finite element analysis, *J. Constr. Steel Res.* 64 (6) (2008) 680–688, <https://doi.org/10.1016/j.jcsr.2007.12.003>.
- [24] M. Pecce, F. Rossi, The experimental behavior and simple modeling of joints in composite MRFs, *Eng. Struct.* 105 (2015) 249–263.
- [25] A. Elkady, D.G. Lignos, Modeling of the composite action in fully restrained beam-to-column connections: implications in the seismic design and collapse capacity of steel special moment frames, *Earthq. Eng. Struct. Dyn.* 43 (13) (2014) 1935–1954, <https://doi.org/10.1002/eqe.2430>.
- [26] L.F. Ibarra, R.A. Medina, H. Krawinkler, Hysteretic models that incorporate strength and stiffness deterioration, *Earthq. Eng. Struct. Dyn.* 34 (12) (2005) 1489–1511.
- [27] D.G. Lignos, Sidesway Collapse of Deteriorating Structural Systems under Seismic Excitations, Stanford university, 2008.
- [28] D.G. Lignos, H. Krawinkler, Deterioration modeling of steel components in support of collapse prediction of steel moment frames under earthquake loading, *J. Struct. Eng.* 137 (11) (2011) 1291–1302, [https://doi.org/10.1061/\(asce\)st.1943-541x.0000376](https://doi.org/10.1061/(asce)st.1943-541x.0000376).
- [29] H. El Jisr, A. Elkady, D.G. Lignos, Composite steel beam database for seismic design and performance assessment of composite-steel moment-resisting frame systems, *Bull. Earthq. Eng.* 17 (6) (2019) 3015–3039, <https://doi.org/10.1007/s10518-019-00564-w>.
- [30] H. El Jisr, A. Elkady, D.G. Lignos, Hysteretic Behavior of Moment-Resisting Frames Considering Slab Restraint and Framing Action, *J. Struct. Eng.* vol. 146 (8) (2020), [https://doi.org/10.1061/\(asce\)st.1943-541x.0002696](https://doi.org/10.1061/(asce)st.1943-541x.0002696).
- [31] EN 1993-1-1, Eurocode 3: design of steel structures—part 1–1: General rules and rules for buildings, European Committee for Standardization, Brussels, 2005.
- [32] EN 1994-1-1, Eurocode 4: Design of composite steel and concrete structures – Part 1.1: General rules and rules for buildings, European Committee for Standardization, Brussels, 2004.
- [33] EN 1998–3, Eurocode 8: Design of structures for earthquake resistance - Part 3: Assessment and retrofitting of buildings, European Committee for Standardization, CEN, Brussels, 2005.
- [34] AISC 341–16, Seismic Provisions for Structural Steel Buildings, American Institute for Steel Construction, Chicago, 2016.
- [35] AIJ, Recommendation for limit state design of steel structures, 3rd ed., Architectural Institute of Japan, Tokyo, 2010.
- [36] A.Y. Elghazouli, M. Kumar, P. Stafford, Prediction and optimisation of seismic drift demands incorporating ground motion frequency content, *Bull. Earthq. Eng.* 12 (1) (2014) 255–276.
- [37] M. Kumar, J.M. Castro, P.J. Stafford, A.Y. Elghazouli, Influence of the mean period of ground motion on the inelastic dynamic response of single and multi degree of freedom systems, *Earthq. Eng. Struct. Dyn.* 40 (3) (2011) 237–256.
- [38] M. Kumar, P.J. Stafford, A.Y. Elghazouli, Influence of ground motion characteristics on drift demands in steel moment frames designed to Eurocode 8, *Eng. Struct.* 52 (2013) 502–517.
- [39] M. Kumar, P.J. Stafford, A.Y. Elghazouli, Seismic shear demands in multi-storey steel frames designed to Eurocode 8, *Eng. Struct.* 52 (2013) 69–87.
- [40] M. Bravo-Haro, A. Tsitos, A.Y. Elghazouli, Drift and rotation demands in steel frames incorporating degradation effects, *Bull. Earthq. Eng.* 16 (10) (2018) 4919–4950.
- [41] A. Tsitos, M.A. Bravo-Haro, A.Y. Elghazouli, Influence of deterioration modelling on the seismic response of steel moment frames designed to Eurocode 8, *Earthq. Eng. Struct. Dyn.* 47 (2) (2018) 356–376.
- [42] A.Y. Elghazouli, J.M. Castro, B.A. Izzuddin, Seismic performance of composite moment-resisting frames, *Eng. Struct.* 30 (7) (2008) 1802–1819, <https://doi.org/10.1016/j.engstruct.2007.12.004>.
- [43] ABAQUS, *Analysis User's Manual, Version 2017*. DSS (Dassault Systèmes Simulia Corp), Providence, RI, USA, 2017.
- [44] E.P. Popov, R.M. Stephen, Cyclic loading of full-size steel connections, Center for Cold-Formed Steel Structures Library, 112 (1972).
- [45] C. Gilton, B. Chi, C.-M. Uang, Cyclic response of RBS moment connections: weak-axis configuration and deep column effects, in: Department of Structural Engineering, University of California, San Diego, 2000.
- [46] P. Clark, K. Frank, H. Krawinkler, R. Shaw, Protocol for fabrication, inspection, testing, and documentation of beam-column connection tests and other experimental specimens, in: SAC Steel Project Background Document. October, Report No. SAC/BD-97/02, 1997.
- [47] O. Bursi, G. Gramola, Behaviour of composite substructures with full and partial shear connection under quasi-static cyclic and pseudo-dynamic displacements, *Mater. Struct.* 33 (3) (2000) 154–163.
- [48] C. Doneux, H. Parung, A study on composite beam-column subassemblages, in: Proceedings of the 11th ECEE Conference, Paris, 1998.
- [49] K. Udagawa, H. Mimura, Behavior of composite beam frame by pseudodynamic testing, *J. Struct. Eng.* 117 (5) (1991) 1317–1334.
- [50] L.-H. Han, W. Li, Seismic performance of CFST column to steel beam joint with RC slab: experiments, *J. Constr. Steel Res.* 66 (11) (2010) 1374–1386.
- [51] ECCS, Recommended testing procedure for assessing the behaviour of structural steel elements under cyclic loads, in: European Convention for Constructional Steelwork Brussels, Belgium, 1986.
- [52] EN 10034:1993, Structural steel I and H sections-Tolerances on shape and dimensions, European Committee for Standardization, Brussels (1993).
- [53] J. Lemaître, J.-L. Chaboche, *Mechanics of Solid Materials*, Cambridge university press, 1994.
- [54] H. Krawinkler, N.G. Cofie, H. Hadidi-Tamjed, B. Lashkari-Irvani, M. Zohrei, Recommendation for Experimental Studies on the Seismic Behavior of Steel Components and Materials, Stanford University, John A. Blume Earthquake Engineering Center, 1983.
- [55] E. Kaufmann, B. Metrovich, A. Pense, Characterization of cyclic inelastic strain behavior on properties of A572 Gr. 50 and A913 Gr. 50 rolled sections, 2001.
- [56] K. Nip, L. Gardner, C. Davies, A.Y. Elghazouli, Extremely low cycle fatigue tests on structural carbon steel and stainless steel, *J. Constr. Steel Res.* 66 (1) (2010) 96–110.
- [57] EN 1992-1-1, Eurocode 2: Design of concrete structures - Part 1–1: General rules and rules for buildings, European Committee for Standardization, Brussels, 2004.
- [58] J. Lubliner, J. Oliver, S. Oller, E. Onate, A plastic-damage model for concrete, *Int. J. Solids Struct.* 25 (3) (1989) 299–326.
- [59] J. Lee, G.L. Fenves, Plastic-damage model for cyclic loading of concrete structures, *J. Eng. Mech.* 124 (8) (1998) 892–900.
- [60] CEB/FIB, *Model Code 2010-Final draft*, International Federation for Structural Concrete, Lausanne, Switzerland, 2010.
- [61] B. Sahin, M. Bravo-Haro, A.Y. Elghazouli, Cyclic modelling of composite steel-concrete members, in: *Earthquake Risk and Engineering Towards a Resilient World SECED2019*, Greenwich, London, 2019.
- [62] A. Tsitos, A.Y. Elghazouli, Evaluation of loading protocols for assessing local seismic demands in steel buildings designed to EC8, in: Proc., 16th World Conf. on Earthquakes 16WCEE, International Association for Earthquake Engineering, 2017.
- [63] M. Rahnama, H. Krawinkler, Effects of soft soil and hysteresis model on seismic demands, John A. Blume Earthquake Engineering Center Stanford, 1993.
- [64] S. Mazzoni, F. McKenna, M.H. Scott, G.L. Fenves, OpenSees command language manual vol. 264, Pacific Earthquake Engineering Research (PEER) Center, 2006.

- [65] A. Elkady, D.G. Lignos, Analytical investigation of the cyclic behavior and plastic hinge formation in deep wide-flange steel beam-columns, *Bull. Earthq. Eng.* 13 (4) (2015) 1097–1118.
- [66] A.Y. Elghazouli, J. Treadway, Inelastic behaviour of composite members under combined bending and axial loading, *J. Constr. Steel Res.* 64 (9) (2008) 1008–1019.
- [67] M. Araújo, L. Macedo, J.M. Castro, Evaluation of the rotation capacity limits of steel members defined in EC8-3, *J. Constr. Steel Res.* 135 (2017) 11–29.
- [68] EN 1998-1-1, Eurocode 8: Design of Structures for Earthquake Resistance, Part 1–1: General Rules and Seismic Action - Working Draft, 2020.
- [69] B. Sahin, M. Bravo-Haro, A.Y. Elghazouli, Influence of composite action on the inelastic behaviour of composite steel-concrete members, in: 17th World Conference on Earthquake Engineering, 17WCEE, Sendai, Japan, 2020.
- [70] C.-M. Uang, C.-C. Fan, Cyclic stability criteria for steel moment connections with reduced beam section, *J. Struct. Eng.* 127 (9) (2001) 1021–1027.
- [71] T.B. Panagiotakos, M.N. Fardis, Deformations of reinforced concrete members at yielding and ultimate, *Struct. J.* 98 (2) (2001) 135–148.
- [72] P.E. Mergos, K. Beyer, Loading protocols for European regions of low to moderate seismicity, *Bull. Earthq. Eng.* 12 (6) (2014) 2507–2530.